

© 2021 Eric Alpine

PRELIMINARY DESIGN OF THE DARKNESS MISSION  
FOR FERMI NATIONAL ACCELERATOR LABORATORY

BY

ERIC ALPINE

THESIS

Submitted in partial fulfillment of the requirements  
for the degree of Master of Science in Aerospace Engineering  
in the Graduate College of the  
University of Illinois Urbana-Champaign, 2021

Urbana, Illinois

Adviser:

Clinical Associate Professor Michael Lembeck

## ABSTRACT

This thesis presents the preliminary design of a 6U CubeSat satellite for the Fermi National Accelerator Laboratory (Fermilab). The satellite incorporates components from NanoAvionics, LLC and supports a pair of charged-coupled devices (CCDs) with high energy resolution to characterize a 3.5 keV X-ray signal hypothesized to be associated with dark matter. The “Dark matter as a sterile NEutrino Search Satellite” (DarkNESS) is a collaboration between Fermilab and with the University of Illinois Department of Aerospace Engineering’s Laboratory for Advanced Space Systems at Illinois (LASSI).

DarkNESS is a challenging mission with significant interplay between thermal control, power generation, orbit selection, instrument pointing configuration, and communications bandwidth. Mission analysis was developed for multiple DarkNESS configurations and bounded by the potential launch opportunities to Sun-synchronous or low-inclination orbit environments. The analysis identified durations of Earth obscuration of the instrument field of view and evaluated imaging opportunities when a suitable observation window was available in Earth’s eclipse. View factor computations informed the assessment of the external heating of the instrument aperture and radiator surfaces. A compact cryocooler is required to achieve the operating temperature of the instrument focal plane (170 K). The mission analysis incorporated the cryocooler in a finite element model to evaluate the internal and external heating and simulated the steady-state focal plane temperature for the instrument.

The following steps for DarkNESS include thermal control risk mitigation tests to validate the cryocooler and radiator design integration and completion of a critical design review. The launch of DarkNESS to low earth orbit is anticipated in early 2024.

## ACKNOWLEDGMENTS

I am fortunate to have encountered several individuals who left positive influences on my academic career. The submission of this thesis is a realization of a long-sought, and once seemingly unattainable, goal. To my professors, Dr. Michael Lembeck and Dr. Zackary Putnam, thank you. I have had the opportunity to pursue my ambitions because of your guidance and investment.

This research was made possible with funded support from the Fermi National Accelerator Laboratory. I am grateful to program sponsor Juan Estrada and Fermilab for the unique opportunity to contribute to the DarkNESS mission. I'd also like to thank Stephanie Timpone, who initiated the working relationship between Fermilab and the University of Illinois. I'd like to acknowledge Dr. David Carroll of CU Aerospace, who coordinated program management and contractual efforts with the University. Their support has provided a generation of LASSI undergraduate and graduate students with invaluable experience in satellite design.

I'd like to thank Brent Abbott and NanoAvionics for the positive working relationship and product support.

To my LASSI partners, Hongrui Zhao, Michelle Zosky, and Chris Young, for all the late nights working on the things we love. It is a joy.

To my parents, thank you for letting me find my way.

*Ayizuola, through you, my motivation is found. Forever unconditional.*

## TABLE OF CONTENTS

<b>CHAPTER ONE: INTRODUCTION .....</b>	1
<b>CHAPTER TWO: BACKGROUND.....</b>	3
<b>CHAPTER THREE: LITERATURE REVIEW.....</b>	8
<b>3.1 Recent Applications of Space-based Cryogenic Instruments.....</b>	8
<b>3.2 Case Studies of Cryogenic Devices on Small Satellites .....</b>	10
<b>3.2.1 Thermal Shielding for Small Satellites.....</b>	10
<b>3.2.2 Integrated Dewar Cooler Assembly for a Small Satellite .....</b>	14
<b>3.2.3 Cryocooler Demonstration Case Study .....</b>	17
<b>CHAPTER FOUR: DARKNESS MISSION REQUIREMENTS.....</b>	22
<b>4.1 Stakeholder Requirements .....</b>	23
<b>4.2 Concept of Operations .....</b>	25
<b>4.3 The DarkNESS Scientific Instrument .....</b>	30
<b>CHAPTER FIVE: MISSION ANALYSIS.....</b>	32
<b>5.1 Process Overview .....</b>	32
<b>5.2 Obstruction Analysis.....</b>	34
<b>5.3 Earth-Radiator View Factor Analysis.....</b>	47
<b>5.4 Radiator and Aperture Ambient Heating.....</b>	52
<b>CHAPTER SIX: THERMAL ANALYSIS .....</b>	59
<b>6.1 Process Overview .....</b>	59
<b>6.2 DarkNESS Thermal Model .....</b>	62
<b>6.3 Thermal Model Performance Results .....</b>	67
<b>CHAPTER SEVEN POWER ANALYSIS .....</b>	72
<b>7.1 Process overview .....</b>	72
<b>7.2 Power Subsystem Sizing .....</b>	73
<b>CHAPTER EIGHT: DATA AND COMMUNICATIONS.....</b>	80
<b>8.1 Process Overview .....</b>	80
<b>8.2 DarkNESS Radio Options and Link Budget .....</b>	81
<b>8.3 Ground Station Options .....</b>	83
<b>CHAPTER NINE: CONFIGURATION.....</b>	84
<b>9.1 Process Overview .....</b>	84
<b>9.2 DarkNESS Mass Budget.....</b>	84

<b>9.3 DarkNESS Configuration.....</b>	<b>87</b>
<b>CHAPTER TEN: CONCLUSION AND ACTION ITEMS .....</b>	<b>92</b>
<b>REFERENCES.....</b>	<b>94</b>

## **CHAPTER ONE: INTRODUCTION**

In Spring of 2020, Fermi National Accelerator Laboratory (Fermilab) approached the Laboratory for Advanced Space Systems at Illinois (LASSI) within the University of Illinois' Aerospace Department to assess interest and capability in developing a small research satellite. The proposed research focused on the detection of a candidate particle decay theorized to be associated with dark matter. Fermilab's science team outlined their mission objective to characterize a potential signal detected by the European Space Agency's (ESA) Multi-Mirror X-ray Newton observatory (XMM-Newton) and confirmed by NASA's Chandra X-ray observatory. It is hypothesized that the signal may be the result of the decay of large sterile neutrinos, a type of neutrino predicted to be associated with dark Matter [2][3][5].

Powerful ground-based telescopes are unable to further characterize the signal due to atmospheric interference and attenuation. The DarkNESS instrument, developed by Fermilab, features two wide Field-of-View (FOV) Charged Couple Devices (CCDs) with high energy resolution. The CCDs carry heritage from previous observatory science. They served as the primary focal plane on the Blanco 4-meter telescope at the Cerro Tololo Inter-American Observatory located in northern Chile. The instrument is capable of higher resolution exposures than current X-ray telescopes [1][3]. The Fermilab team believes these specialized detectors can discern the desired signal if deployed in the space environment.

A concept study was prepared and presented to Fermilab by LASSI in April 2020. The study provided details of the engineering services available to design a CubeSat bus system for accommodating Fermilab's science payload. LASSI is staffed by undergraduate and graduate students and overseen by a dedicated Director and laboratory manager. LASSI provided systems

engineering services and defined a preliminary program plan for developing the DarkNESS CubeSat bus, payload integration and testing, and mission operations.

A work statement was established to develop a mission responsive to Fermilab's mission-level science requirements and proposed concept of operations. A systems requirement review presented the architectural decomposition of the functional and physical bus hardware requirements. A follow-on systems definition review presented system design configuration options and subsystem trade studies. The use of a.i Solutions' Free-Flyer astrodynamics software aided in evaluating a matrix of parameters for each of the individual configurations. A 6U CubeSat with dual-deployable solar arrays emerged from this system definition process that satisfied the mission level requirements while providing compliant performance. A preliminary design review for this configuration was presented to Fermilab in May 2021. This thesis details the effort that culminated in that review.

## CHAPTER TWO: BACKGROUND

In the 1990s, NASA deployed the first in a series of powerful space telescopes in pursuit of exploring natural phenomena in the observable universe. This first observatory, the Hubble Space Telescope (HST), conducted observations in the visible region of the electromagnetic spectrum and captured exposures that would otherwise be unachievable from ground-based telescope platforms. With observations unobstructed by Earth's atmosphere, HST collected valuable data that provided insight into the processes of the birth and the death of stars, the evolution of galaxies, and provided evidence used to confirm the existence of black holes. The program known as *The Great Observatories* deployed three additional space telescopes to collect observations across the entire electromagnetic spectrum. Designed to study radiation emissions in the X-Ray band, the Chandra observatory deployed a highly sensitive X-Ray telescope that further contributed to investigations of the universe's origin, evolution, and physical density. The telescope made possible more detailed observations of X-Ray emitting natural bodies leading to discoveries in the fields of high-energy physics, gravitation, and cosmology [5].

One significant contribution made by the Chandra mission involved the confirmation of a particular X-Ray signal detected by the European Space Agency's (ESA) Multi-Mirror X-Ray Newton observatory (XMM-Newton) [2]. As part of ESA's Horizon 2000 program, the X-Ray telescope is similar in design and objective to the Chandra observatory and performed numerous narrow and broad-range spectroscopy observations of X-Ray emitting sources. An unidentified emission line was detected through the analysis of stacked X-Ray spectra from groups of galaxy clusters. Led by the Harvard-Smithsonian Center for Astrophysics, the discovery published in *The Astrophysical Journal* suggests the existence of an emission line at 3.55-3.57 keV and is shown in Figure 1. The signal discovered by analysis on the stacked spectra captured by XMM-

Newton of 73 galaxy clusters was also detected by Chandra when observing the Perseus Cluster. Analysis of subdivided spectra-set reveals an emission line greater than  $3\sigma$  statistical significance [2].

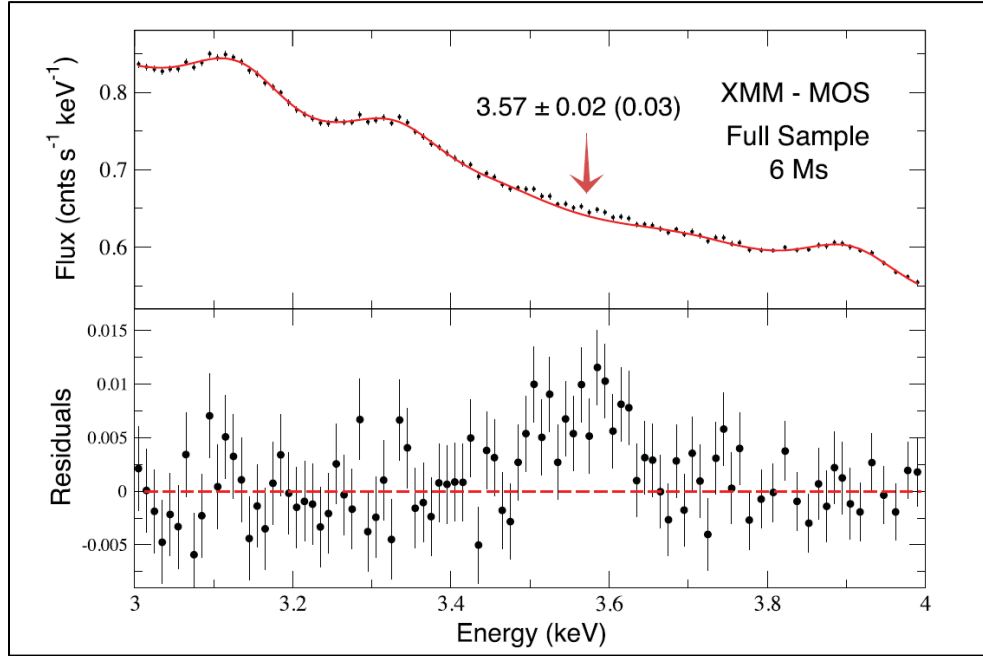


**Figure 1** The 3.5 keV signal found in the stacked samples from XMM-Newton MOS spectrum observations [2].

The discovery of the 3.5 keV X-ray signal is of interest to theoretical physicists, as it is not recognized as an emission from any known atomic transitions found in observable intra-cluster mediums. Such medium consists of superheated gas composed primarily of ionized hydrogen and helium. This baryonic plasma is enriched with heavier elements and emits radiation as X-rays through energy transition when valence shells of excited elements decay [41]. The emission lines from the emitting plasma bodies can be detected and characterized by X-ray telescopes (Figure 2), providing a means of understanding the intragalactic medium's structural composition that bounds galactic clusters. In the case of Chandra and XMM-Newton observatories, the signal emitted from multiple galaxy clusters was distinguishable over the background radiation environment.

Background radiation introduces noise in the spectra and can prevent weak signals from being discerned if the detector's resolution is inadequate. The detection of the 3.5 keV signal is at the limit of any currently available X-ray observatories' instrument resolution, presenting a challenge in further investigating the potential discovery signal that exists within a range of 50 to 110 eV of other known emitting plasma elements [2][3][7][41].

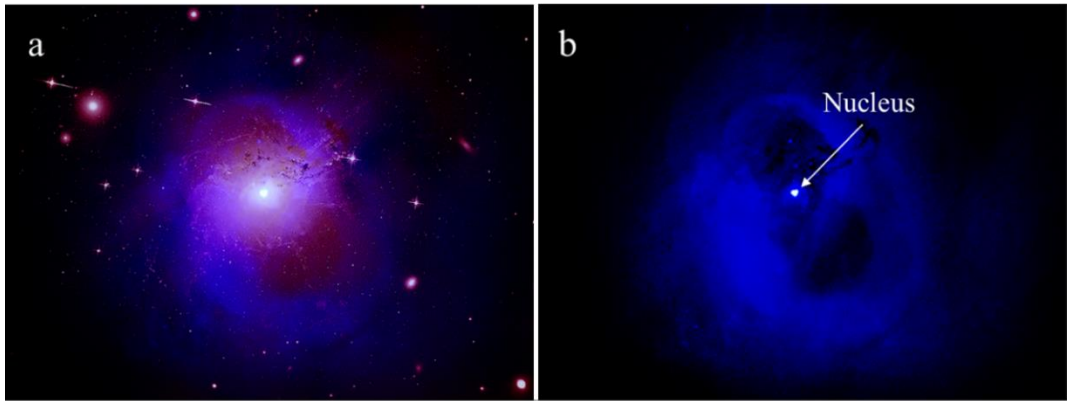


**Figure 2 (a) Composite image of the Perseus Cluster combining X-ray, Optical, and Radio exposures. (b) X-ray image of the Perseus Cluster and Nucleus made by the Chandra Advanced CCD Imaging Spectrometer [8].**

One theory suggests that dark matter exists in association with sterile neutrinos. The sterile neutrino is a theoretical particle differentiated by its interaction with the fundamental forces. Unlike other neutrinos, which can interact through the electroweak force, the theory suggests that the sterile neutrino only interacts through the gravitational force. One indicator that supports this interpretation is derived from the relative strength of the detected signal. It is unlikely to be the consequence of any misidentified atomic transition, as the distribution of the heavier, non-baryonic species would require it to exist in greater abundance than other enriching elements, such as Potassium, within the intra-cluster medium. It is not believed that such a species would be widespread in galaxies like the Milky Way. Another consideration is the difficulty in detecting the potential particle that emits the discovery signal. The lack of interaction with the fundamental

forces, except gravity, is consistent with the interpretation of the observation. The sterile neutrino is a potential candidate particle believed to be associated with the distribution of dark matter about galactic nuclei and the emitter of the unresolved 3.5 keV discovery signal [2][7]. The generalized mechanism of the decay process of the sterile neutrino is illustrated in Figure 3.

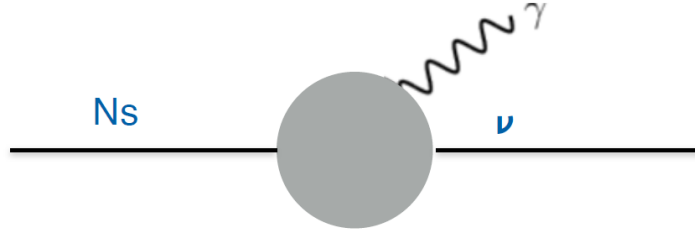


**Figure 3** A photon is emitted in the form of an X-ray as the sterile neutrino ( $N_s$ ) decays into a standard neutrino ( $\nu$ ) [9].

Resolving weak X-ray lines requires the observations to obtain long-duration and unobscured exposures of galactic regions, feature the proper energy resolution on the instrument focal plane, and provide a wide FOV to characterize the signal properly. Since current X-ray telescopes have a narrow FOV and lack the necessary energy resolution to resolve the weak X-ray lines, alternate observation methods have resorted to instruments such as X-ray microcalorimeters aboard experimental sounding rockets. Although these microcalorimeters have wide FOV and collect spectra comparable in sensitivity of sizeable effective-area telescopes, the trajectories of sounding rockets result in short duration observations. Short duration exposures, available from sounding rocket experiments, fail to provide the adequate observation time required to perform the necessary signal integration, making a satellite platform the best candidate to further the science investigation [4].

The proposed detector features two customized CCDs with dimensions on the order of 10 cm<sup>2</sup>. This sizing makes a CubeSat platform attractive for hosting the mission. One stand-out challenge is maintaining and controlling the detectors' cryogenic operating temperature. The focal plane of the detector operates at 170 K to minimize thermal noise. An adequate thermal solution will influence significant portions of the trade space and consist of passive and active design elements. To minimize thermal cycling that could lead to instrument failure, a thermal solution that can maintain a 5 K gradient over the detector's focal plane for long durations is desired. While the power and mechanical specifications of the payload detector are well-suited for the CubeSat platform, the thermal operating conditions imposed by the detector significantly influence the design of the satellite.

## CHAPTER THREE: LITERATURE REVIEW

Maintaining the instrument operating temperature required by the DarkNESS mission is a challenge for a 6U CubeSat. The instrument's CCD focal plane temperature must be maintained at  $170\text{ K} \pm 5\text{ K}$  while observing [6]. While passive components such as radiators, heat-sinks, and thermal straps may contribute to the thermal management of the instrument, active methods are required to chill and maintain the focal plane at the specified operating temperature.

Small satellites that follow the CubeSat design standards are limited by mass, volume, and power generation when sizing a thermal control system incorporating active components. Before developing a thermal control solution for DarkNESS, a review of the literature covering current cryogenic or near-cryogenic space science applications was undertaken.

### 3.1 Recent Applications of Space-based Cryogenic Instruments

DarkNESS performs galactic observations using two high-resolution soft X-ray CCD detectors in the low Earth orbit environment. The application of cryogenic devices on satellite platforms has advanced in recent years, resulting in broad community interest in implementing cooling systems on CubeSats like DarkNESS [10].

Technology advancements in low-temperature superconductors have resulted in various microdevices with improved resistance to thermal cycling and consistent electrical performance. Applications of the technology has benefited instrument thermal control system design enabling progress in astrophysical science investigations. Components such as superconducting tunnel junctions, superconducting quantum interference devices, resonating cavities, and low losses RF filters are examples of the technology improvements enabling high-performance instrument designs for use in the space environment [10].

The first space-based X-ray Observatory, NASA's *Einstein* mission, was deployed into low Earth orbit in 1978 and contained a suite of scientific instruments, including a solid-state spectrometer with a silicon lithium detector. The spectrometer analyzed soft X-ray signals in the 0.5 to 4.5 keV energy range and required an operational temperature of 100 K. Thermal control of the spectrometer was achieved by mounting the instrument to a coldplate interface within an ammonia and methane cryostat [12]. The application of cryostat-based thermal control systems remains prevalent in many large-platform astrophysics missions. Space telescopes such as NASA's Cosmic Background Explorer (COBE), and more recently, the James Webb Space Telescope feature similar cryostat technologies.

The application of cryogenic detectors on satellite platforms has advantages over the use of alternate sensor technologies. Cryogenic detectors provide higher sensitivity, measured by noise equivalent power and an increased energy resolution. These benefits drive the system design of various instrument technologies, including CCD-based photon detectors, to provide the resolving power required to perform high-resolution astronomical observations [10]. Research into the development of cryogenic systems for CubeSats has only recently been considered. Table 1 lists some characteristics of applicable cryogenic CCD-based detector technologies for potential astrophysics missions [10].

**Table 1 CCD Characteristics [10]**

Parameter	Value
Spectral Range	Visible/X-ray ( $1E-10 < \lambda < 1E-6$ )
Temperature Range	150 K – 300 K
Power Dissipation Range	0.1W to 20 W
Detector Size (Pixel / Array)	10-30 $\mu\text{m}$ / $10E6 (\text{nxn})$

## **3.2 Case Studies of Cryogenic Devices on Small Satellites**

The following three case studies survey the state of the art of cryogenic devices operating on CubeSat platforms. Implementation of passive and active thermal control schemes is considered to chill and maintain the Fermilab instrument focal plane temperature at 170 K. The cases pertain to CubeSat systems that have recently launched or are under active development.

### **3.2.1 Thermal Shielding for Small Satellites**

Passive thermal control components requiring no additional power are preferred for CubeSats. A joint program between NASA's Kennedy Space Center and Sierra Lobo Inc. recently launched into LEO in February 2020 to demonstrate a passive shielding system to radiatively cool a payload by exposure to the ambient "cold" space environment [13][22]. The 3U satellite, called CryoCube-1, featured an experiment canister filled with pressurized oxygen and chilled to 120 K by preventing radiative sources from illuminating the canister and allowing the gaseous oxygen to condense into a liquid [14].

The passive cooling strategy used by CryoCube-1 relies on a rigid-frame deployable structure encapsulated in flexible silver aluminized Multi-Layer Insulation (MLI). The experiment is also equipped with a sensor suite to study the behavior of cryogenic fluids in the micro-gravity environment. The 3U satellite containing the exposed canister and an engineering drawing of the deployed reflective shielding is provided in Figure 4 [13][14].

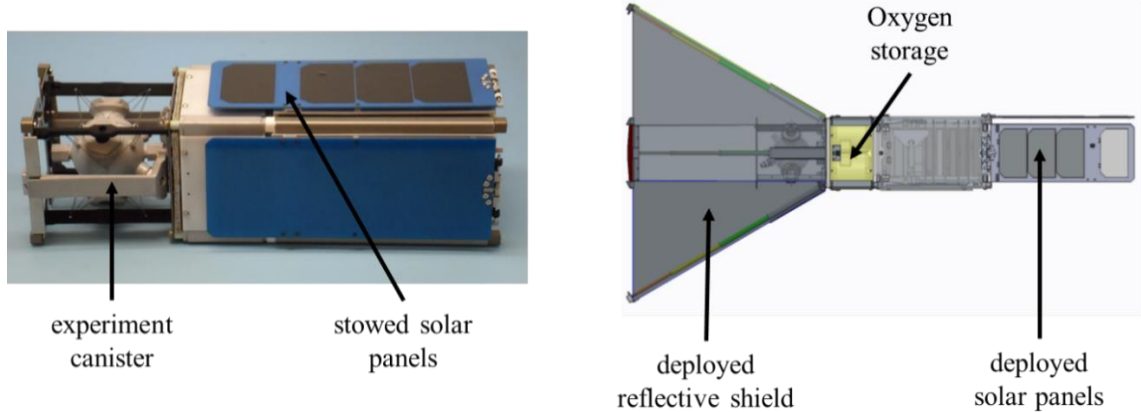


**Figure 4** *CryoCube-1 satellite and payload configurations [14].*

Sierra Lobo performed thermal modeling on CryoCube-1 to predict its passive shielding performance in the space environment. The model analyzed the oxygen tank temperature in a simulated LEO space environment, allowing temperature gradients across the satellite to be calculated. The preferred CubeSat orientation (Figure 5), aligns the z-axis (defined from the center of the satellite and points through the experiment canister) away from the Sun vector and towards dark space at all times [14]. The satellite maintains the desired orientation by rolling about the perpendicular body x-axis, rotating the experiment canister away from the Sun at the orbital rotation rate. The deployable shielding reflects radiation from the Sun and Earth that would otherwise illuminate the experiment [13][14].

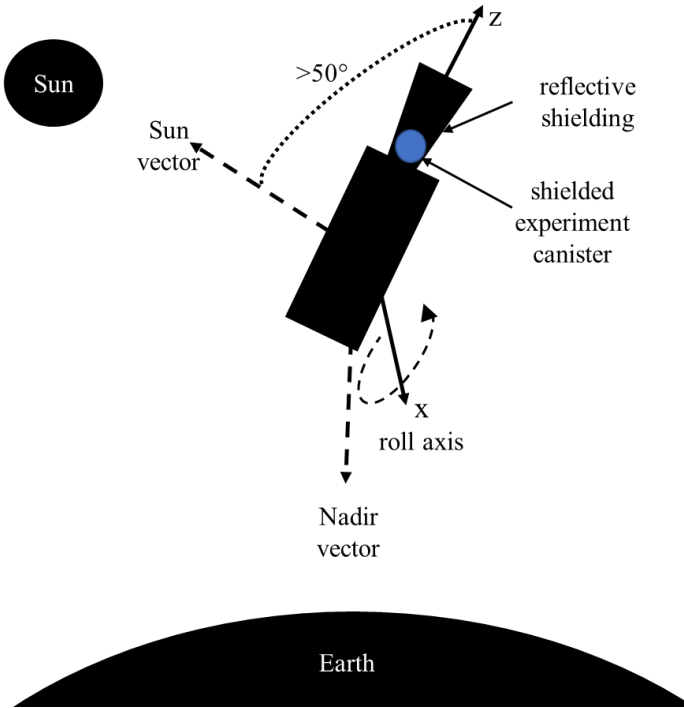


**Figure 5 Ideal CryoCube-1 science orientation [14].**

The deployable thermal shielding performance was modeled for CryoCube-1 using two tools, Thermal Desktop and Comsol Multiphysics, for orientations bound by the solar vector and orbit plane. Table 2 lists two bounding cases used in the simulation. In the first case, the angle between the z-axis and the solar vector, shown in Figure 5, is maintained at 60 degrees. The canister reaches a steady-state temperature of 80 k over 3.5 days by holding this configuration. In the second case, the angle between the z-axis and the solar vector is reduced to 40 degrees, allowing illumination of the experiment canister, resulting in the canister steady-state temperature increasing to 104 K.

**Table 2 CryoCube-1 Steady State Canister Temperature [14]**

Case	Configuration	Canister Temperature (Steady State)
1	z-axis/orbit plane angle: 60° Solar vector/orbit plane angle: 60°	80 k (in 3.5 days)
2	z-axis/orbit plane angle: 40° Solar vector/orbit plane angle: 0°	104 k (in 3.5 days)

The thermal simulation of CryoCube-1 provides a case study on thermal shielding to chill experiment components passively. The canister is outfitted with several small LEDs for controlled illumination during imaging sessions, an internal pressure sensor, and temperature, level, and mass measurements provided by Sierra Lobo's Cryo-Tracker® system. A total of 20 mW of heat is dissipated by these components [14]. As shown in Figure 6, the experiment canister can dissipate the 20 mW heat load, allowing a passive-only thermal management system to be used.

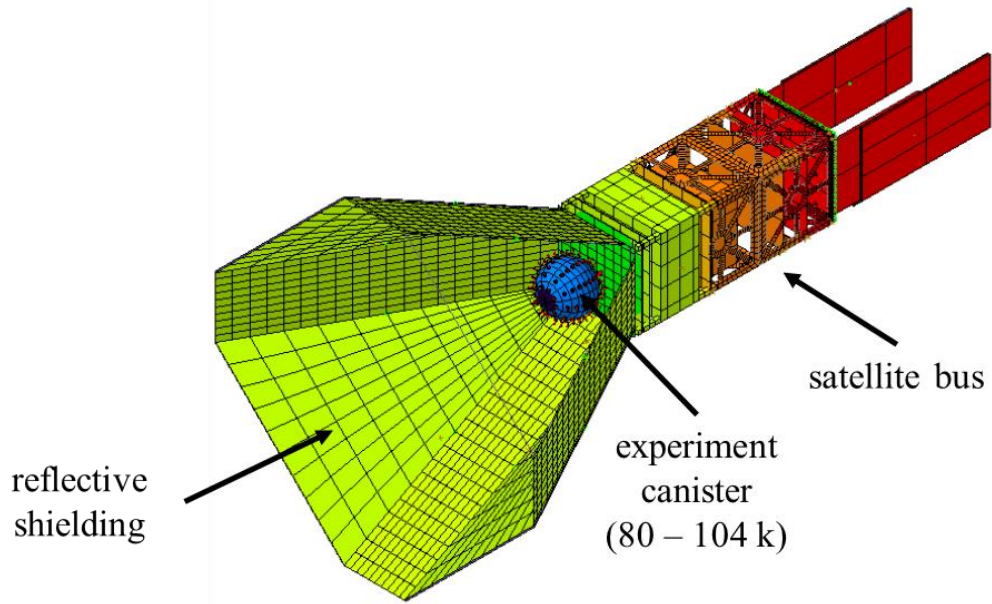


**Figure 6 shows the thermal gradient of CryoCube-1 from analysis performed in Thermal Desktop and Comsol Multiphysics software [14].**

The use of thermal shielding to prevent illumination was shown to be effective for CryoCube-1. However, it may be insufficient for other applications if the shielded component dissipates a more significant heat load, as is expected for the Fermilab instrument. MLI may be considered to reduce thermal exposure of internal components, such as heat radiated from other satellite subsystems.

### **3.2.2 Integrated Dewar Cooler Assembly for a Small Satellite**

The application of compact cryogenic devices in remote sensing instruments has enabled CubeSat platforms to be used as low-cost tools for satisfying research objectives. At the Hawaii Space Flight Laboratory at the University of Hawaii at Manoa, another program has integrated a Hyperspectral Thermal Imager (HyTI) for deployment on a 6U CubeSat platform. The mission, funded by the In-Space Validation of Earth Science Technologies (InVEST) program from NASA's Earth Science Technology Office, is a technology demonstration of a hyperspectral imager aiming to perform high spectral and spatial resolution long-wave infrared observations. The payload, displayed in Figure 7, will capture spectra-radiometrically calibrated images using a spatially modulated interferometric imaging technique and is scheduled for launch in Fall 2021 onboard a 6U CubeSat [15][16][17]. The science objective is of interest to the University's Hawaii Institute of Geophysics and Planetology to further study the thermal properties of the Earth's surface. The payload features a novel Fabry-Perot interferometer with no moving parts and uses the high-performance Barrier Infra-Red Detector (BIRD) developed by JPL. The Focal Plane Array (FPA) area is roughly  $400 \text{ mm}^2$  and requires a cryogenic operating temperature of 68 K [15][16].

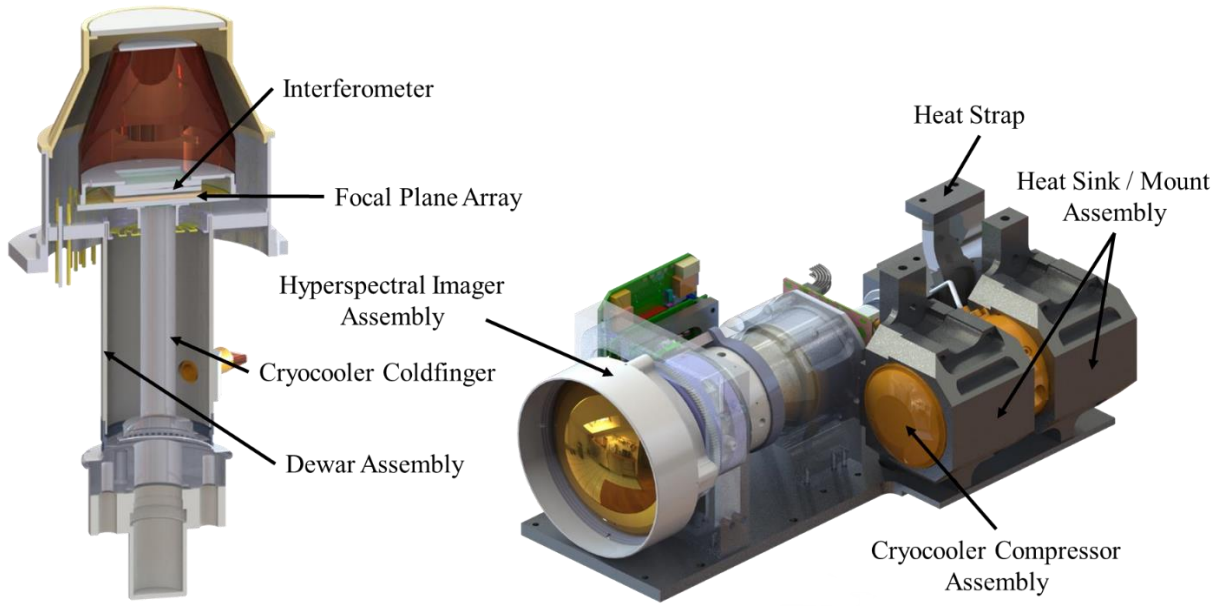


**Figure 7 Hyperspectral thermal imager integrated with a cryocooler assembly and JPL's T2SLS BIRD FPA [17].**

The active cooling method applied to the detector FPA is significant as it is integrated with the payload detector assembly and operated on the 6U CubeSat platform. The lightweight and compact Stirling cryocooler (Figure 8) extracts heat from the detector mount. The device is a commercially available component from AIM Infrared-Module and is compatible with an Integrated Dewar Cooler Assembly (IDCA) [15][16][18]. The SF070 model cryocooler has a rated cooling power of 0.4 W @ 80 K in an ambient temperature of 71°C and is applied to chill the FPA to achieve acceptable dark current levels [15].

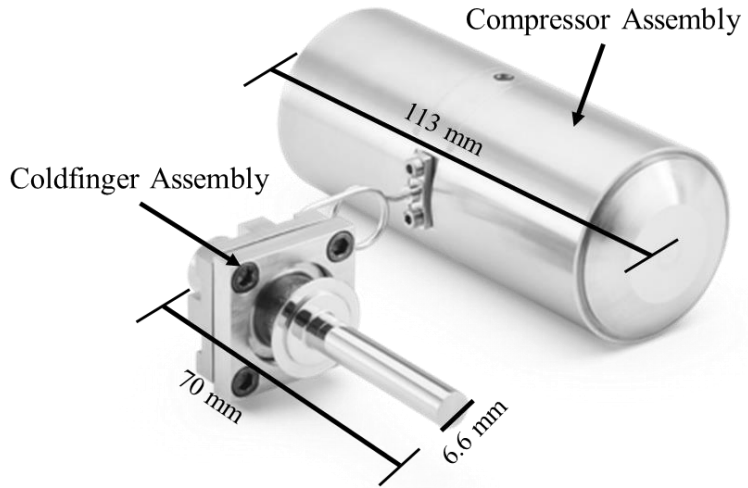


**Figure 8 AIM SF070 Stirling Cryocooler used in the HyTI 6U satellite to chill a detector focal plane array [15][16][18].**

The SF070 cryocooler has a mass of approximately 850 grams and requires an input voltage of 5 to 15 V. With a maximum performance cooling power of 0.4 W, the device can manage detector temperature requirements in the range of 70 to 140 K [18]. The cryocooler is interfaced directly to the underside of the BIRD FPA assembly and contained within the header portion of a Dewar housing.

Power requirements for the HyTI payload and bus subsystems are provided in Table 3 from the Hawaii Spaceflight Laboratory. Maximum power consumption ranges from 16 to 63 W, with the most significant users being the cryocooler and payload avionics [17]. The power required to chill the FPA from ambient to operating temperature is approximately 45 W over 10 minutes. The cryocooler maintains the FPA temperature, requiring 22 W over the same period. In total, the payload imager operates for 20 minutes per imaging cycle, consuming a total energy capacity of 11 Whrs to hold the ~400 mm<sup>2</sup> FPA at 68 K [17].

**Table 3 HyTI Payload and Subsystems Power Requirements [17]**

Component	Approximate Power Consumption [W]
Cryocooler Active	45
Cryocooler Maintain 68K	22
Payload Imager	3
Payload Avionics	10 – 30
Bus	5
ADCS Slew	3
Communications	12
<b>Total</b>	<b>16 – 63</b>

The case of the HyTI program provides an overview of the performance merits of a cryocooler onboard a 6U CubeSat. While the FPA is smaller than the DarkNESS focal plane, measuring roughly 3,600 mm<sup>2</sup> versus HyTI's 400 mm<sup>2</sup> BIRD FPA, the project shows that the 6U platform design accommodated a compact cryocooler. Further consideration becomes necessary to evaluate a similar cryocooler's capacity to chill the larger focal plane of the DarkNESS instrument, presenting a unique challenge in integrating a compact cryocooler with increased focal plane areas. The use of compact cryocoolers is considered further in the final project case.

### 3.2.3 Cryocooler Demonstration Case Study

A final case study examines the Active CryoCubeSat (ACCS), shown in Figure 9. ACCS is a program between Utah State University and NASA's Jet Propulsion Laboratory. The concept provides a prototype for high-power CubeSats using a two-stage Active Thermal Architecture (ATA) featuring a Mechanically Pumped Fluid Loop (MPFL) to radiate heat from an internal heat exchanger to dark space [19].

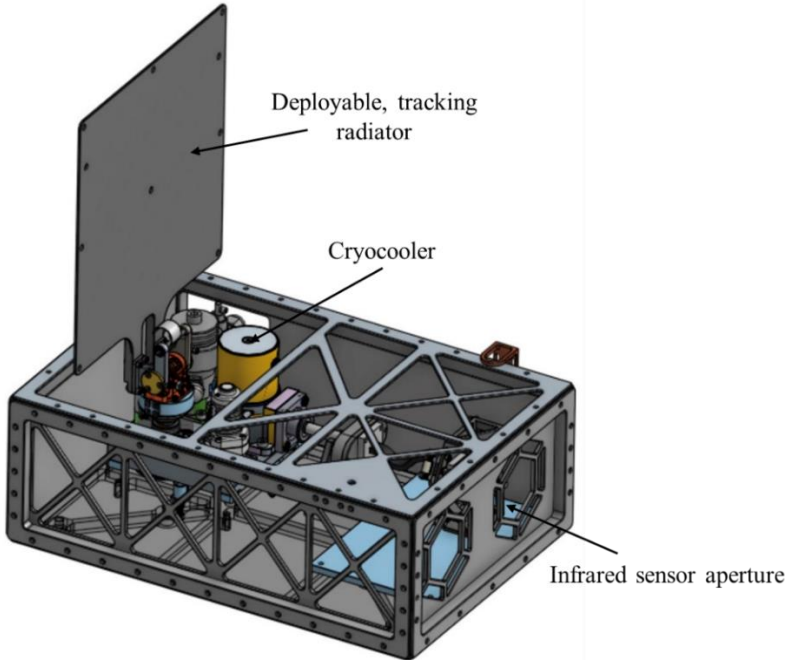


**Figure 9** The 6U ACCS prototype with the integrated active thermal architecture [20].

The ATA is designed for small satellites and utilizes a compact cryocooler to satisfy an infrared sensor's thermal requirements. An integral rotary K508N cryocooler, commercially available from Ricor, makes up the second stage of the ATA and interfaces to the heat exchanger of the fluid loop. The cryocooler chills the infrared sensor to 70 to 120 K and dissipates an average internal heat load of 10 Watts to maintain the sensor's operating temperature [19]. The heat generated from the cryocooler is transferred into the working fluid through the heat exchanger and pumped through a deployable radiator tracking dark space, as depicted in Figure 10.

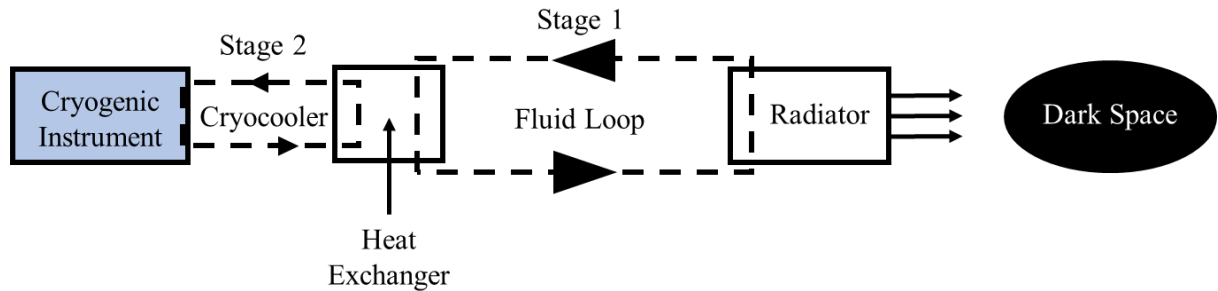


**Figure 10** ACCS active thermal control architecture [19].

The cryocooler mounting interface (Figure 11) attaches to the heat exchanger of the ATA. Heat is transported from the instrument sensor attached to the coldfinger. The cryocooler's cooling power depends on the mounting interface's temperature and the ATA's capacity to transport and radiate the heat with the MPFL. The first-stage cycling of the working fluid between the heat exchanger and radiator conditions the cryocooler to operate as the second stage cryogenic thermal control for the infrared sensor [19][20].

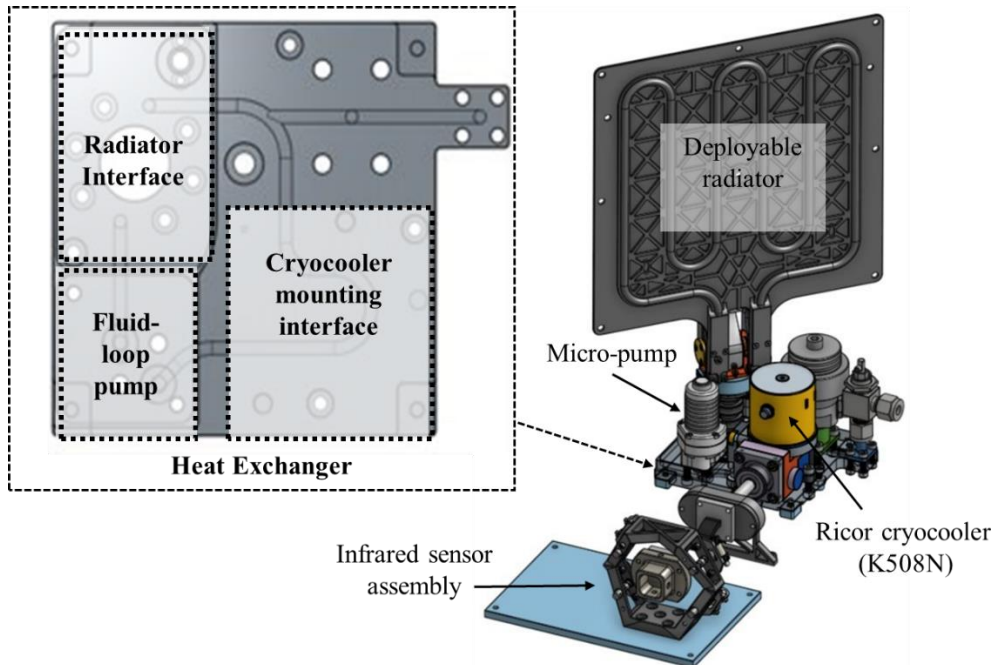


**Figure 11 The active thermal architecture hardware prototype [20]/[21]**

The heat transfer capacity of the MPFL drives the cryocooler's performance. The Ricor K508N can remove a heat load of 1350 mW (applied to the coldfinger) when the mounting interface is 23°C (Table 4). Under these conditions, the coldfinger tip can be maintained at 150 K and requires a cryocooler regulated input power of 11 W. At a warmer mounting interface temperature of 71°C; the cryocooler can maintain the coldfinger tip at 150 K and reject an 1100

mW heat load for an equivalent input power. The mounting interface measures 21 cm<sup>2</sup>, with the fluid-loop removing an 8 to 13W heat load, depending on the cryocooler input power [19][21].

**Table 4 Ricor K508N Cryocooler Reference Bounds [21]**

Coldfinger target temperature (K)	Ambient/Interface Temperature (°C)	Allowable Heat Load (mW)	Regulated Input Power (W)
80	23	650	~ 11
80	71	550	~ 11
150	23	1350	~ 9
150	71	1100	~ 9

To maximize the cooling power of the coldfinger, the ATA must adequately remove the heat load from the cryocooler. The capacity of the fluid-loop to transfer energy out of the system is a design characteristic tuned for the attached device. Utah State University assessed the cryocooler performance with the ATA using two modeling methods.

First, a physical model incorporating each ATA component's thermal characteristics and material interfaces was simulated using *MATLAB SIMSCAPE*. The physical model predicts the average temperature of the heat exchanger and considers the MPFL characteristics. The second method uses system identification to produce a linear model from Thermal Vacuum (TVAC) test data. The average heat exchanger temperature was evaluated by comparing the linear and physical models against the average temperatures recorded during environmental testing. The MPFL maintained the average heat exchanger between -15°C and 15°C [19]. The cryocooler maintained the coldfinger temperature in a range of 100 to 120 K, but the thermal fluctuation of the heat exchanger oscillated significantly. A control scheme using a PID controller to adjust the MPFL flow rate was implemented to mitigate the thermal oscillation using the micropump. The controller stabilized the heat exchanger interface temperature to the cryocooler, maintaining a more consistent cryocooler input power and operating condition.

The ACCS prototype demonstrated an active thermal control approach for small satellites to condition a cryocooler supporting a cryogenic instrument. Active systems such as ATA have the potential to mitigate the significant power dissipation associated with devices such as the Ricor cryocooler. The available cooling power is maximized by the management of the cryocooler mounting interface at cooler temperature ranges. The information available from the ACCS project, particularly the performance of the Ricor cryocooler, helped to inform DarkNESS design efforts.

## CHAPTER FOUR: DARKNESS MISSION REQUIREMENTS

The primary DarkNESS mission objective is to detect and characterize a 3.5 keV signal identified in previous observations of galactic clusters. If the emission is produced by the decay of the theorized sterile neutrino, then its distribution may be correlated to the spatial distribution predicted for dark matter. Dark matter may be concentrated in the vicinity of black holes, and the black hole at the center of our galaxy, Sagittarius A\*, is a convenient target to observe from Earth [1]. By deploying specialized X-ray detectors into a low Earth orbit (LEO), long-duration observations of the center cross-section of the Milky Way can be obtained (Figure 12).

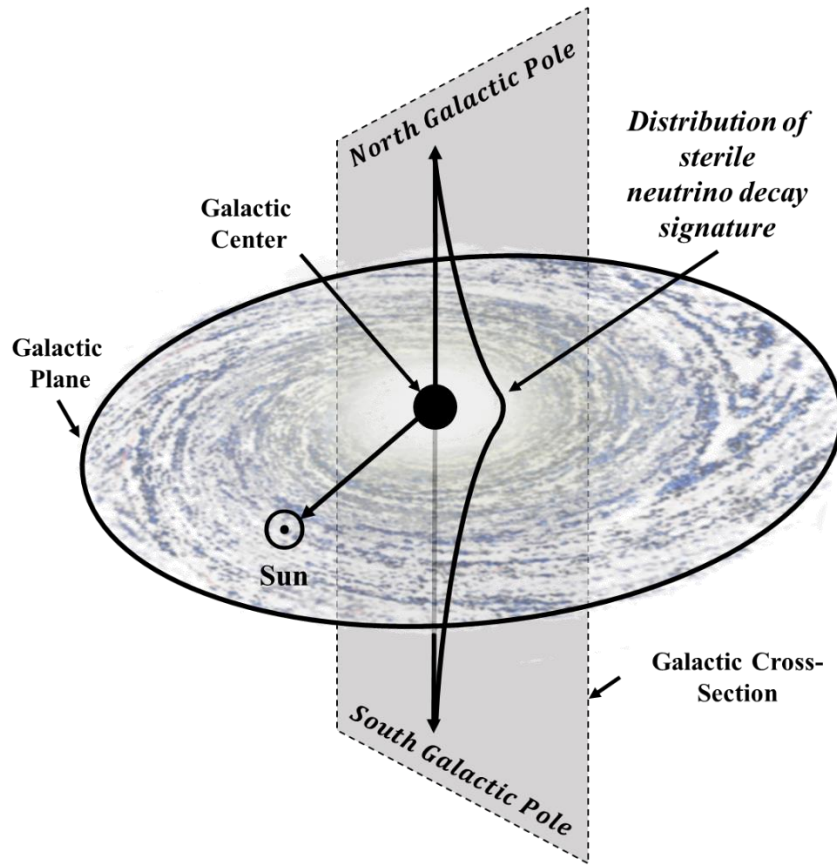


*Figure 12. Representation of the sterile neutrino decay signature about the cross-sectional region of the Milky Way galaxy. Dark matter may concentrate in the vicinity of the galactic center and reveal itself as the 3.5 keV decay signal [1].*

Observational data obtained from the X-ray exposures will be mapped against the theoretical distributions of dark matter around the galactic center. If a correlation exists between the measured and the predicted distributions, the effort will establish evidence supporting the sterile neutrino as a signature particle of dark matter [1][2].

#### **4.1 Stakeholder Requirements**

The principal target of the DarkNESS satellite instrument is Sagittarius A\* (Sag A\*), the black hole at the center of the Milky Way galaxy. Off-target X-ray images will also be collected to assess the distribution of the 3.5 keV signal away from the galactic center, where dark matter should be less concentrated.

Successful collection of science data places constraints on the mission and its orbital parameters. A seasonal constraint is imposed on the mission's science phase to prevent the interference of bright celestial bodies (primarily the Sun and Earth) in the FOV of the X-ray detector. Conditions are most favorable for observations during the seasons marked by the Vernal Equinox and terminating at the Autumnal Equinox. The constraint results in an observation window of approximately 180 days to complete the science data collection objective. An illustration of the seasonal constraint is provided in Figure 13.

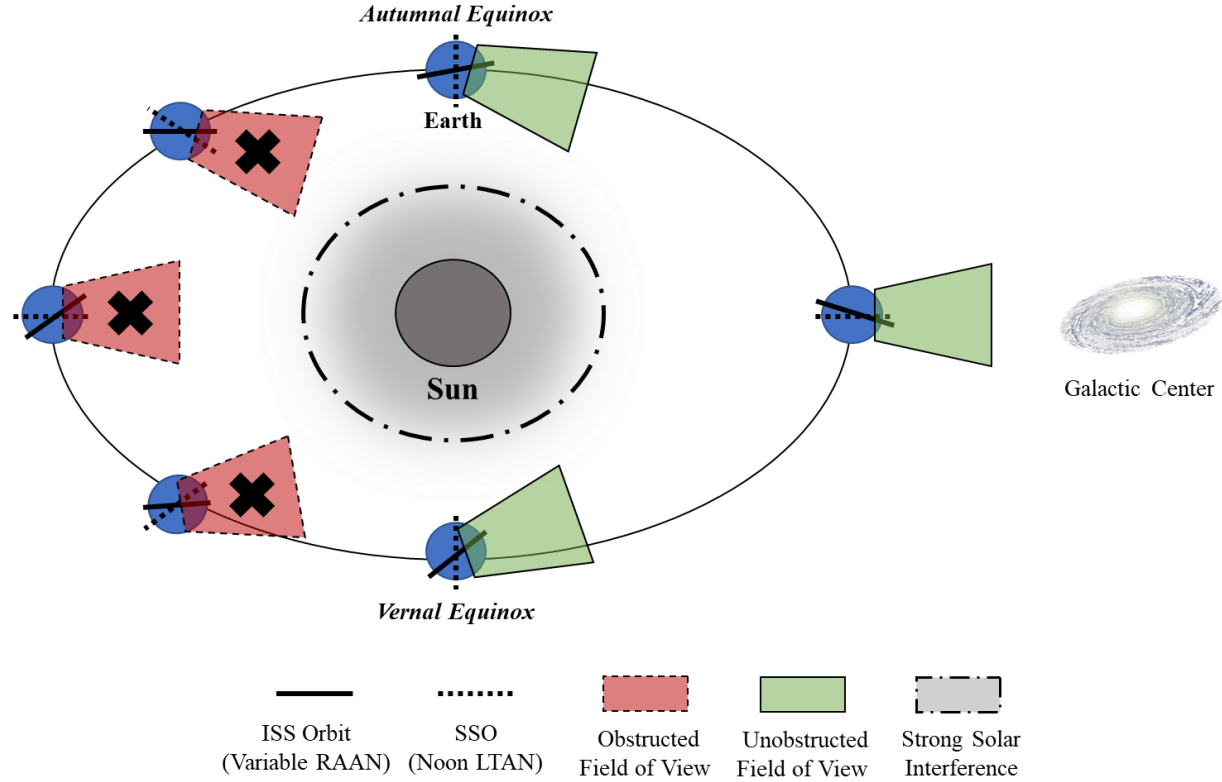


**Figure 13 DarkNESS Seasonal Visibility. Obstruction caused by the Sun limits science data collection to about half a year. The earth may also obscure celestial targets depending on the selected Observatory orbit [9].**

Because the exact launch date of the mission cannot be projected this early in the program, the spacecraft must have a minimum orbital lifetime of one year to guarantee that the observation period is achievable. The resulting set of stakeholder mission requirements are captured in Table 5.

**Table 5 The Principal Stakeholder Science Requirements**

Req. ID	Requirement
MSN-1	<i>The mission shall provide images of celestial targets.</i>
MSN-2	<i>The mission shall provide images within the seasonal duration marked by the Vernal Equinox to the Autumnal Equinox.</i>
MSN-3	<i>The mission shall be designed for a mission duration of no less than 360 days.</i>

## 4.2 Concept of Operations

A Concept of Operations responsive to the stated mission objectives is used to define the system architecture for the mission. The DarkNESS operational concept begins with launching and deploying a small satellite in low Earth orbit (LEO). The satellite and its instrument payload, hereafter referred to as the Observatory, are checked out and readied for the seasonal observation period. Upon passage of the Vernal Equinox, the X-ray detector collects 15-minute exposures of galactic targets in search of the 3.5 keV sterile neutrino decay signal. The satellite points the instrument at celestial targets, maintains the required controlled thermal environment for the X-ray detector, and downlinks science data to Ground Control for scientific analysis. The mission concludes as perturbations naturally decay the satellite's orbit. Components defining the DarkNESS system of systems mission architecture and key mission phases are identified in Figure 14.

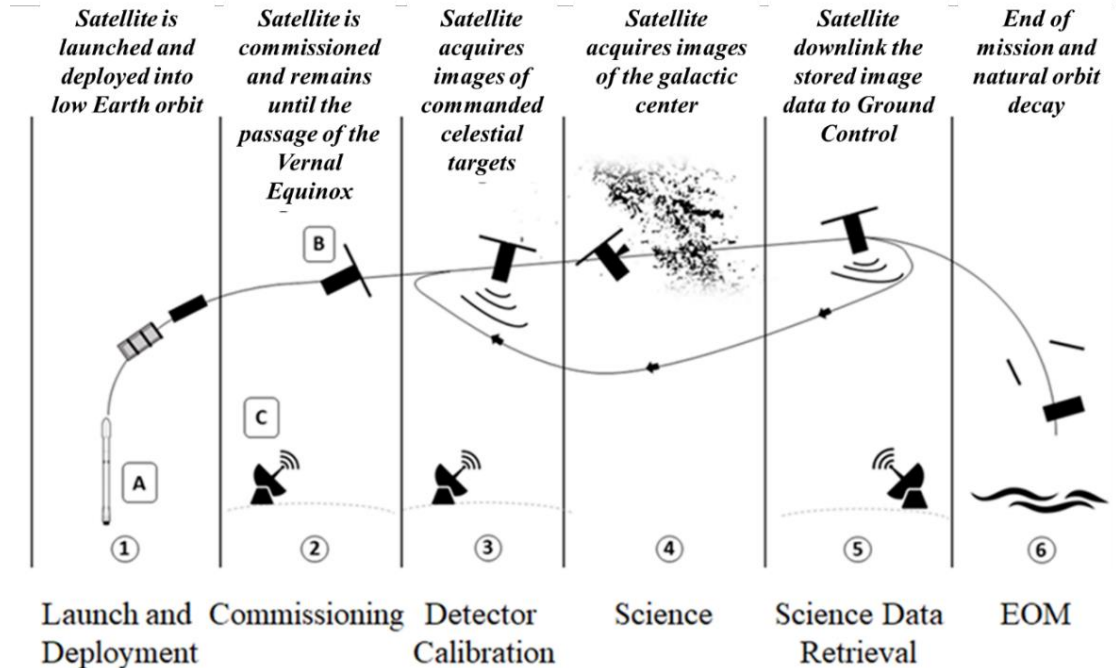


**Figure 14 Mission Concept of Operations.** A small satellite collects x-ray images and relays them to the ground during the seasonal observation period.

The requirements formulation process starts by decomposing the Concept of Operations into a systems architecture which is decomposed into a set of functions that must be performed to accomplish the mission requirements. These functions are then assigned to physical elements required to execute the mission. A launch vehicle is used to place the satellite and instrument payload into orbit. The satellite provides the utilities and services required by the payload to acquire and store images for downlink. A Ground Control station regularly communicates with the satellite to retrieve the captured images and make them available for the mission scientists.

For each of these system elements, specific functions required to achieve the mission objectives, along with required levels of performance for those functions, were defined. Trade studies and analyses were defined to specify performance budgets (e.g., mass, power, communications, data) on the selected hardware to provide these functions. Finally, from these budgets, specifications were developed for the supporting hardware and software elements.

The selection of a Launch Vehicle (and service provider) for the satellite orbital deployment is also influenced by seasonal mission requirements. A launch opportunity is desired close to the start of the observation season to minimize the amount of time the Observatory must spend in orbit prior to collecting data. Launch services that provide sun-synchronous insertions occur less frequently but may allow for more efficient satellite configurations. Launch services that provide International Space Station (ISS) and other LEO deployments may be scheduled more frequently but result in less optimal satellite configurations.

The satellite provides power, pointing, cooling, data collection, and downlink for the scientific instrument payload. Configuration trade studies were formulated to satisfy the mission science objectives and satellite element operation. Several competing factors became evident during these exercises. Solar arrays are used to capture energy from the sun through a large part of

the orbit, yet an external radiator needs to be pointed to deep space away from the Earth and Sun to cool the science instrument focal plane, as illustrated in Figure 15. Attitude control sensors and actuators' field of view compete with the solar array and radiator view angles. All these conflicts must be resolved successfully to achieve the mission science objectives.

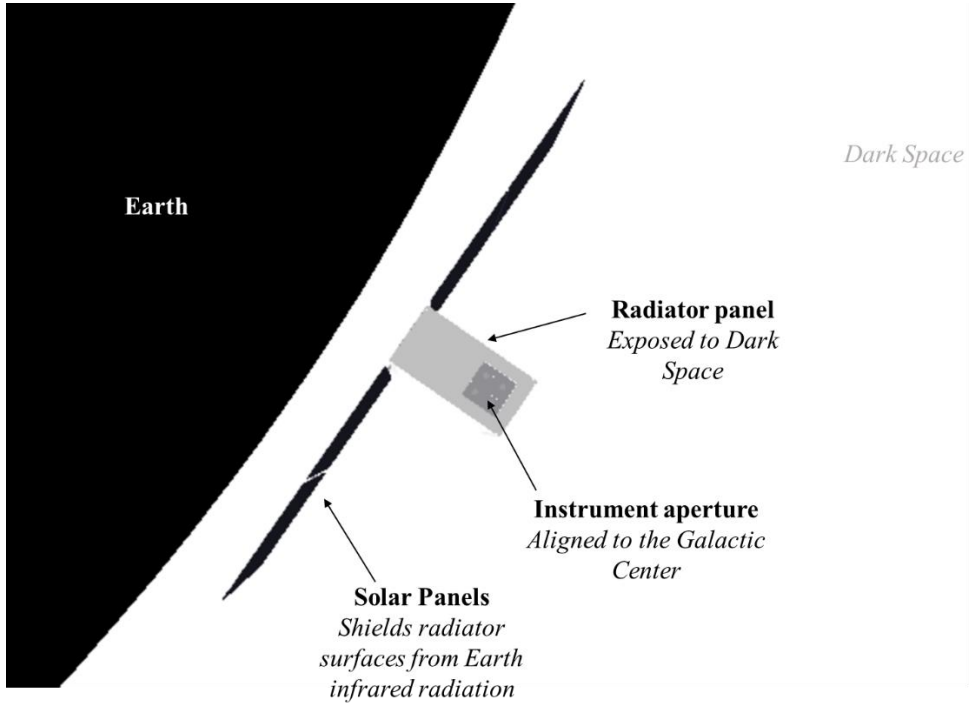


**Figure 15 Alignment of DarkNESS in Earth Eclipse. The instrument aperture is aligned to the galactic center; the satellite rolls about the pointing axis to maximize radiator exposure to dark space [23].**

As detector data is collected, observation images take up a large amount of space in the satellite's memory. The uncompressed image can also be processed into much smaller binned histogram image formats for expedited downlinks. A full image is anticipated to be approximately 25 MB in size and can be broken up into several small packets for downlink over successive orbits. The histogram, however, is expected to be about 2KB in size, and may be downlinked in a single session with the ground station.

Control of the satellite and its operations introduces a third system in the mission architecture called Ground Control. Its functionality can be purchased as a service from a third party or provided by LASSI. Ground Control communicates with the satellite to send and receive instrument payload data and support satellite health and status information. Ground Control also tracks the orbital position of the satellite. The major trade study performed for the ground station establishes the radio band and bandwidth used for radio communications. Larger amounts of instrument data may be downlinked at higher bandwidths. However, supplying higher bandwidths also increases the use of other resources, such as power, on the satellite.

The three major mission elements and their interfaces are provided in Figure 16.

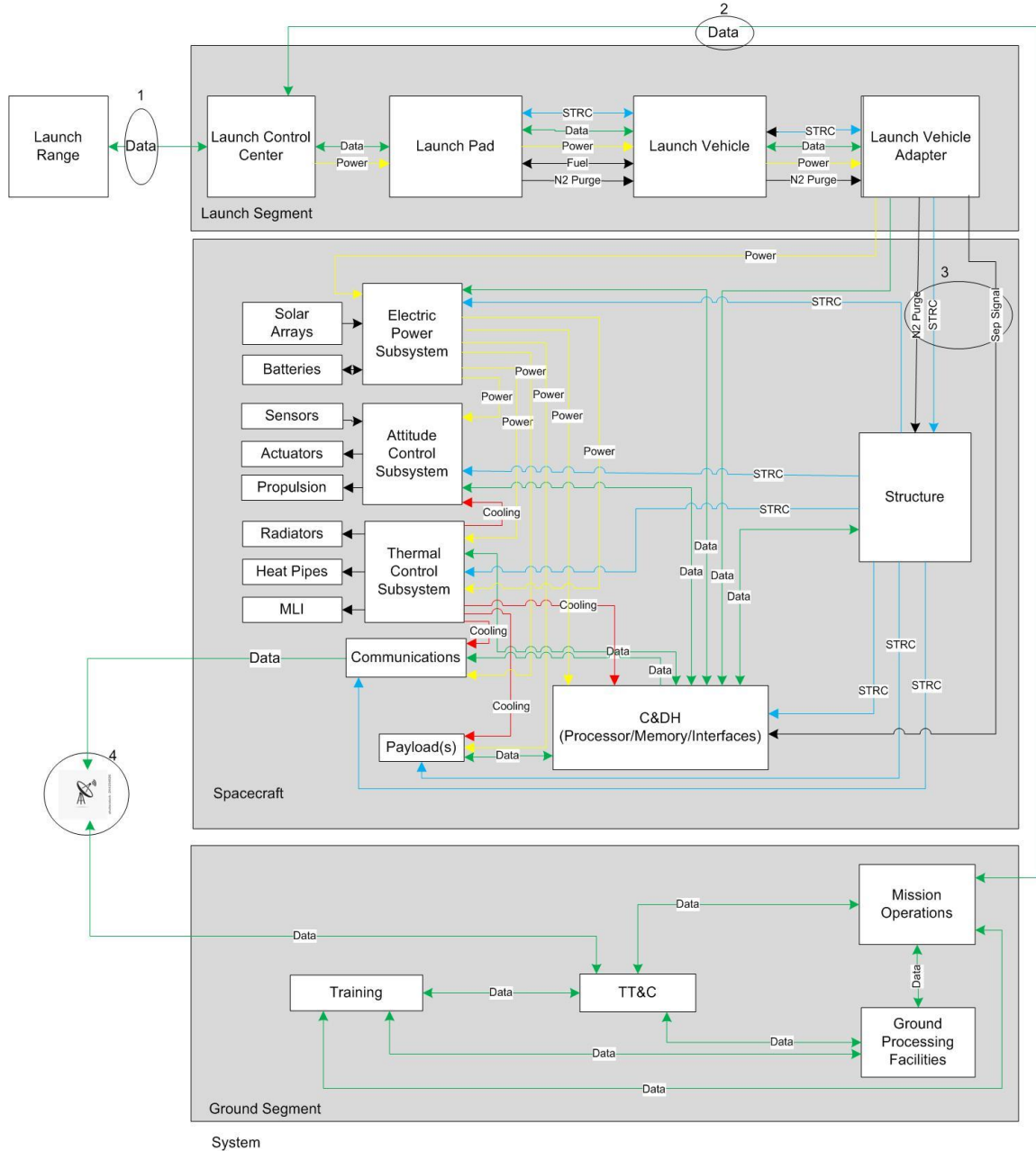


**Figure 16 Notional mission element architecture. The launch vehicle, satellite, and ground station represent the major hardware elements required to meet the DarkNESS mission requirements.**

These major trade studies are defined and explored in the sections that follow, resulting in a preliminary design of the DarkNESS satellite.

### 4.3 The DarkNESS Scientific Instrument

The science instrument driving the mission requirements of DarkNESS was developed by Fermilab and is presented in Figure 17. The main component of the instrument is two 80 Megapixel CCD packages that will image galactic targets. The CCDs require thermal control to maintain an adequate signal-to-noise ratio to detect the weak X-ray decay signature [1]. A Beryllium window assembly overlays the CCDs to restrict lower energy signals from reaching the focal plane. The CCDs are mounted to a coldplate made of aluminum and are chilled by a cryocooler to the required operating temperature of 170 K [1]. The instrument computer, composed of three printed circuit boards, operates the CCDs and collects observation data.

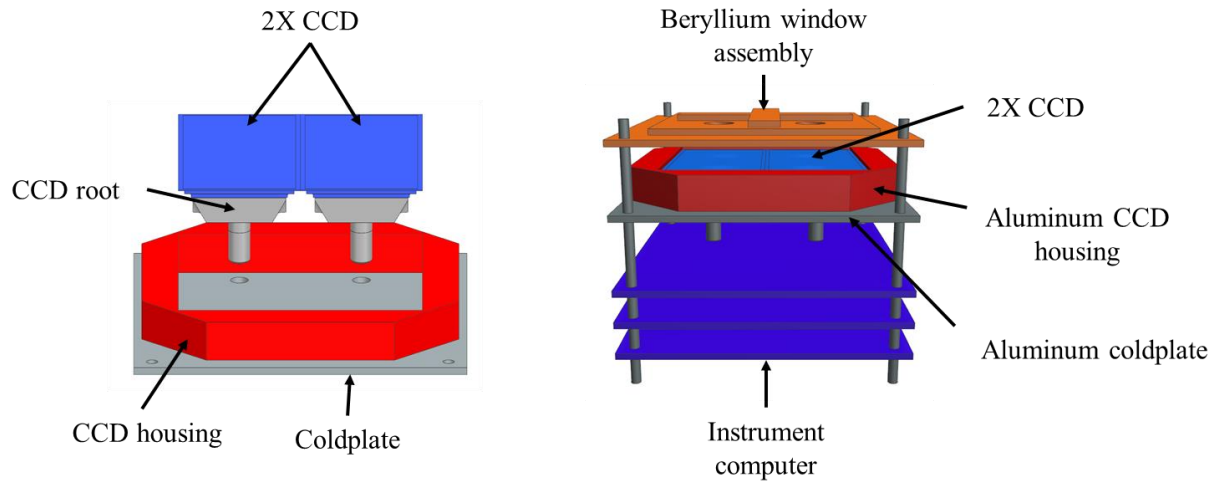


*Figure 17 Key components of the scientific instrument on DarkNESS [42].*

A summary of instrument specifications that drive the requirement-writing process is stated in Table 6.

**Table 6 Summary of the DarkNESS Instrument Requirements [1]**

Performance Requirements	Value
Instrument power load	10 W
CCDs thermal power	0.1 W (each)
Maximum operational sensor temperature	170 K
Allowed temperature variation across the sensor	5 K
Electronics operational temperature range	264 K to 313 K
Observation period	15 minutes/orbit
Pointing accuracy over the observation period	$\pm 5^\circ$
Generated data size, histogram	2.5 KB
Generated data size, image	32 MB
Mass	2 kg

## CHAPTER FIVE: MISSION ANALYSIS

### 5.1 Process Overview

The DarkNESS concept of operations and system architecture was defined by the mission and critical science data collection (Table 7) drivers initially provided by Fermilab.

**Table 7 Key Mission Drivers.** *Design drivers are identified for each mission phase.*

<b>Launch and Deployment:</b> <ul style="list-style-type: none"><li>• The observatory is launched and deployed into low Earth orbit.</li><li>• Bounding orbits include:<ul style="list-style-type: none"><li>◦ International Space Station Deployment (ISS) @ 51.6 deg inclination</li><li>◦ Sun Synchronous Orbit (SSO) @ &gt; 90 deg inclination</li></ul></li></ul>
<b>Commissioning:</b> <ul style="list-style-type: none"><li>• The observatory is commissioned, the orbit is maintained until the start of the Vernal Equinox</li><li>• Launch time may not position satellite for immediate observations (Mar-Jun)</li><li>• Orbital drag may lower orbit significantly from ISS orbit altitude before mission end</li></ul>
<b>Detector Calibration:</b> <ul style="list-style-type: none"><li>• Instrument cooling is initiated, and the instrument commanded to acquire image targets for calibration</li><li>• Instrument focal plane temperature shall be maintained at <math>170 \pm 5</math> K</li><li>• Sensor field of view (FOV) is 40 deg</li></ul>
<b>Science:</b> <ul style="list-style-type: none"><li>• Collect &gt; 500 images of the galactic center over the lifetime of the satellite.</li><li>• Images are collected in 15-minute exposures.</li><li>• Obstruction impact on imaging opportunities</li><li>• Satellite thermal management and radiator panel performance</li><li>• Power generation with solar panels in sunlit orbit</li><li>• Instrument exposure to radiation</li></ul>
<b>Downlink:</b> <ul style="list-style-type: none"><li>• Package information for downlink to Ground Station:<ul style="list-style-type: none"><li>◦ Histograms (small data sets)</li><li>◦ Full-Images (large data sets require high bandwidth downlink)</li></ul></li></ul>
<b>End of mission:</b> <ul style="list-style-type: none"><li>• Natural orbit decay and re-entry</li></ul>

Satellite functional and performance requirements were derived and further evaluated in trade studies. With these requirements driving the overall mission design, a significant amount of the mission analysis was performed in the a.i. Solutions' FreeFlyer astrodynamics software tool to validate the mission concept [23].

The orbit analysis performed for the DarkNESS mission identified constraints imposed by orbital mechanics that impact science data collection. Specifically, impacts caused by celestial geometry on obstruction events (celestial bodies encroaching on the observation target), thermal management (for the satellite and instrument), and power management (solar array pointing) were evaluated. The process took advantage of the custom scripting capabilities available within FreeFlyer to model the view factor calculations of satellite surfaces to determine any obstruction of the science instrument detector by the Earth during imaging sessions and to estimate heat loads on the detector. These view factor outputs were compared to results produced from the DarkNESS thermal model, developed using Siemens NX Thermal software described in Chapter 6, and found to be confirming.

Several candidate DarkNESS configurations were identified for investigation in the analysis. A 3U platform was investigated first but failed to provide adequate radiator surface area and power generation capacity for the mission. The reduced volume further constrained internal subsystem configuration, particularly the configuration of the cryocooler. A 6U CubeSat with deployable solar panels, however, readily satisfied the performance requirements.

Forward and side pointing instrument aperture orientations on the 6U platform were considered in this analysis and shown in Figure 18. The forward pointing configuration ultimately provided maximum radiator area and minimum view obstructions.

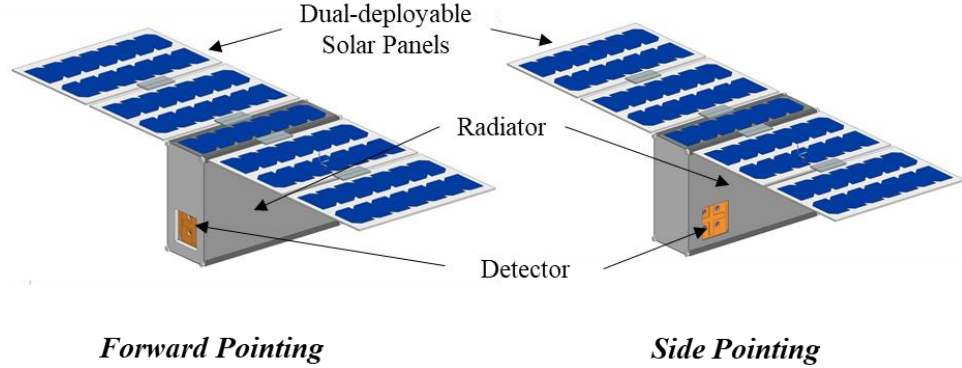


**Figure 18** Two 6U DarkNESS configurations investigated in the mission analysis. Forward pointing offers radiator space and obscuration minimizing advantages.

System mass, power, and data budgets, along with corresponding CAD configurations, also served as inputs for the mission analysis, enabling multiple satellite configurations to be evaluated by a set of performance parameters. Details of this analysis follows.

## 5.2 Obstruction Analysis

The Galactic Coordinate System (GCS) is a useful coordinate frame to describe galactic targets of interest for the DarkNESS science objective (Figure 19). The GCS has a reference plane encompassing the galactic equator, with Sagittarius A\* defining the galactic center. The North Galactic Pole (NGP) lies along a line that passes through the Sun and is perpendicular to the galactic equator. By convention, this point is referenced by a constellation named *Coma Berenices* that is located off the galactic plane. The GCS projects the Milky Way galaxy onto a celestial sphere with the Sun at the center and object coordinates on the sphere mapped by the galactic latitude ( $b$ ) and longitude ( $l$ ) [24].

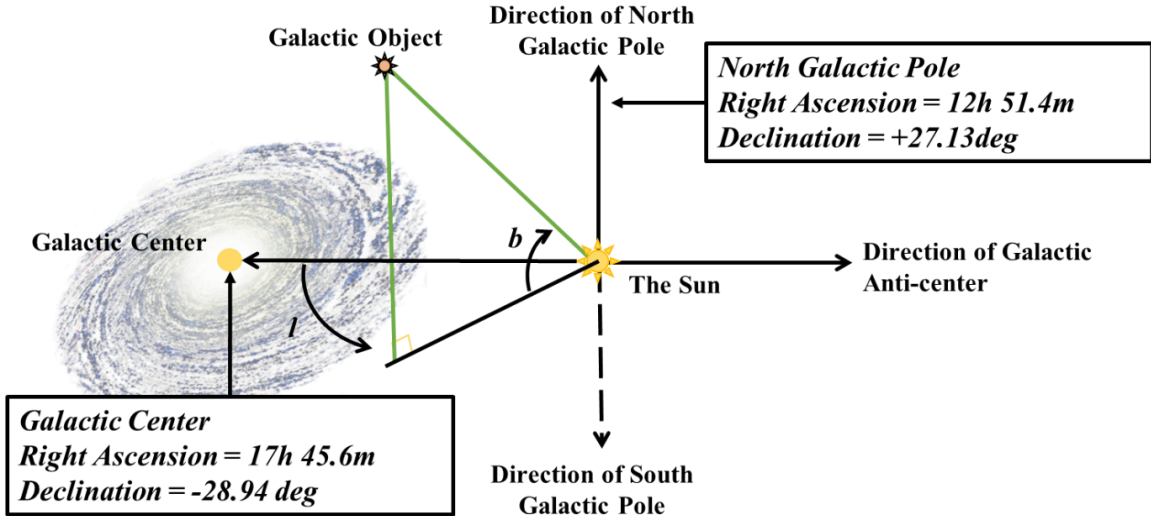


**Figure 19 Galactic Coordinate System. The celestial coordinates (Right Ascension and Declination) for the galactic center and North Galactic Pole. Celestial objects define the coordinate system [24].**

As it relates to the Fermilab science, it is of interest to map the expected intensity of the x-ray signal throughout the cross-section of the galaxy. A coordinate map between the GCS and an Earth-Centered Inertial (ECI) frame provides a simple method to express off-galactic plane observations in a common reference system used in orbit analysis, while science data is better referenced in a celestial frame or GCS.

A seasonal constraint restricts science observations between the Vernal Equinox and the Autumnal Equinox, where the instrument FOV is free from obstruction by the Sun. Obstructions caused by the Earth, however, are affected by the orbit geometry with respect to the Earth. To characterize these obstructions, candidate satellite configurations were simulated with varying orbit geometry for the designated observation period.

Simulation of these orbits accounted for perturbations from natural forces caused by sources such as the non-uniform gravity from Earth's mass distribution, atmospheric drag, tidal

force induced by the moon, and solar radiation pressure. These forces physically act on a satellite and can influence its orbital parameters over time.

While an infinite number of orbital configurations are possible for DarkNESS, two bounding orbit classes, driven principally by launch services available to place DarkNESS in orbit, were analyzed. The first, is an International Space Station (ISS) deployment and is represented by a low-inclination circular orbit with an average altitude of roughly 400 km. The second bounding orbit is a Sun-Synchronous Orbit (SSO) at an altitude of 700 km. The two orbit cases for DarkNESS are illustrated in Figure 20.

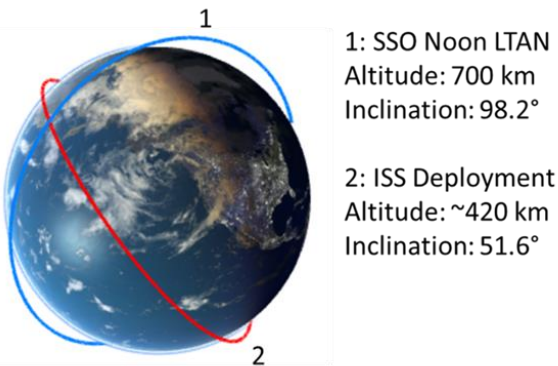


**Figure 20: SSO and ISS orbit cases used in the FreeFlyer analysis of DarkNESS. SSO and ISS orbit configurations help bound obstruction analyses [23].**

Two additional factors were identified that influence instrument obstruction by the Earth. First, the position of the Earth in its orbit around the Sun dictates the geometry between the instrument FOV and the Earth's limb as the instrument points to the galactic center. The second factor is driven by the natural perturbations that influences the orbit geometry with respect to the Earth. While perturbations can influence multiple orbit parameters, the orbit component most associated with the obstruction is the parameter known as the *Right Ascension of the Ascending Node* (RAAN).

The RAAN describes an orientation of an orbit as an eastward angle between the first point of *Aries* (a conventional reference point) to the ascending node of the orbit, illustrated in Figure 21. Perturbations that act on DarkNESS result in the orbit's nodal regression about the Earth throughout the mission life, altering the apparent position of Earth's limb from the perspective of the instrument FOV as it points to the galactic center [25].

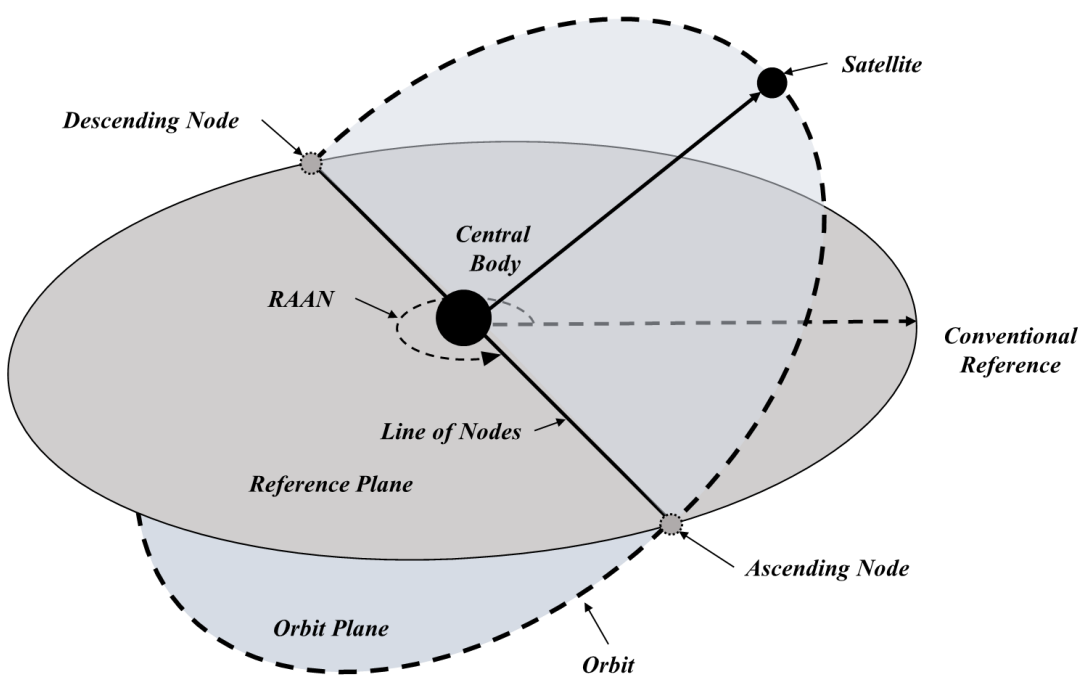


**Figure 21 Orbit Orientation and Orbital Elements.** RAAN is related to the obstruction of the instrument on DarkNESS [25][26].

At the beginning of the science observation window, on the Vernal Equinox, the Sun no longer obstructs the instrument FOV as it is pointed towards the galactic center by the satellite. Depending on the orbit RAAN, however, the Earth may obstruct the FOV for short durations. Obstruction windows are determined by performing simulations with the various orbit and satellite configurations. As the Earth orbits the sun, moving past the Vernal Equinox and into mid-Spring, obstructions caused by the Earth are driven by the nodal regression of the RAAN orbital parameter.

For the mid-latitude ISS and near-polar SSO, the RAAN causes the orbit to regress about the Earth over time. A benefit of the SSO is its nodal regression counteracts the orbital motion of Earth about the Sun by coupling the orbit semi-major axis and inclination. This trade-off is balanced with the frequency of launch availability and cost associated with delivery to the selected orbit. The analysis performed in FreeFlyer assessed the merits of both the ISS and SSO cases for each of the proposed satellite configurations.

Evaluation of obstruction events requires knowledge of the location of the astronomical target being observed and the FOV of the instrument being deployed. In the case of DarkNESS, the instrument FOV is 40 degrees, and the primary science target is the galactic center. An example illustration of a resulting obstruction of the FOV is provided from simulation in Figure 22. The geometry that produced the obstruction is from the SSO case at the Vernal Equinox.

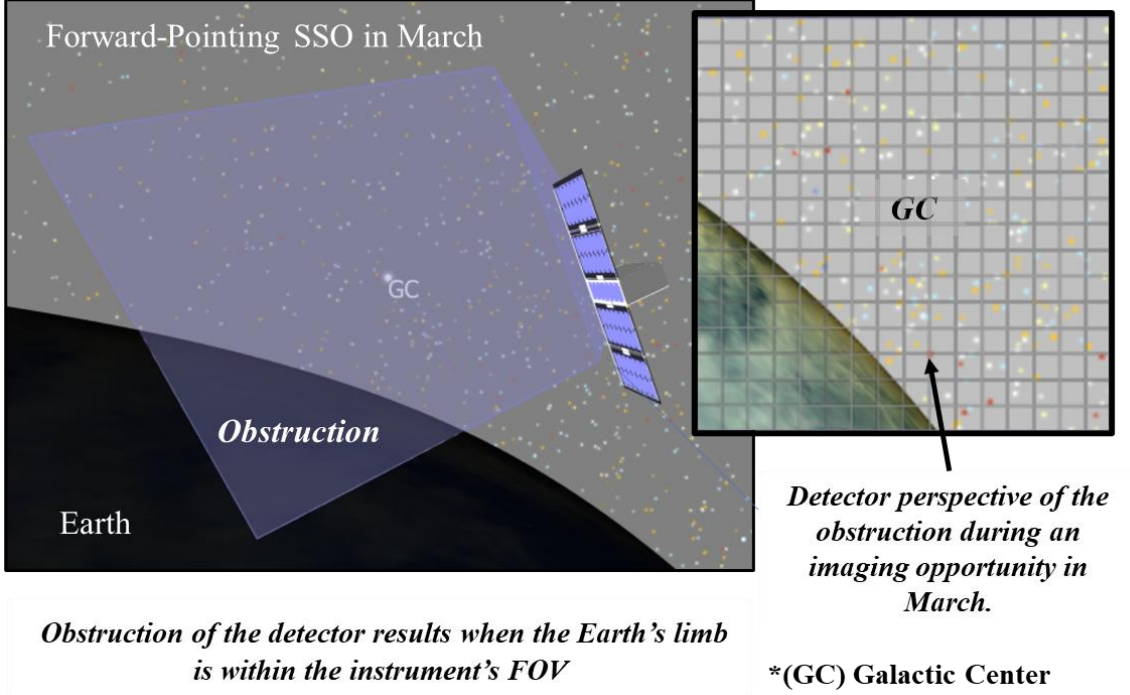


**Figure 22** Obstruction view from FreeFlyer as DarkNESS targets the galactic center. A clear, unobstructed view of the galactic center is desired for long-duration science observations [23].

To evaluate obstruction events for the two satellite configurations (i.e., front and side pointing instrument), a steering algorithm was developed for DarkNESS to point the instrument at observation targets and perform Sun tracking for power collection. DarkNESS images galactic targets only when the satellite passes through the eclipsed orbit region during the science phase. Upon entering the eclipse, the satellite aligns the detector towards the galactic center. When exiting the eclipse, the solar array is pointed at the sun for maximum illumination.

Other satellite orientations are also of interest, leading to a set of pointing modes that have been defined for DarkNESS. These modes control the satellite's attitude depending on the task being performed at particular locations in orbit. The steering algorithm orients the satellite for each of the pointing modes as described in Table 8.

**Table 8 DarkNESS Pointing Modes.** A steering algorithm maintains the satellite's attitude depending on the task being performed.

Pointing Mode	Orientation	Orbit Region
Sun tracking	Point solar panels to the Sun	Sunlit
Detector pointing	Point detector to target	Eclipse
Ground station pass	Points antenna to ground	Passage over ground station
Radiator alignment	Maximize radiator exposure to dark space	Full orbit
Detector alignment	Minimize detector exposure to the earth and sun	Full orbit

Numerical simulations for each satellite configuration were performed for both the SSO and ISS mission orbit options. The simulations implemented in FreeFlyer were initiated at the 2023 Vernal Equinox epoch for each trial with a run time of 180 days, simulating an entire science observation window for DarkNESS. Gravitational, atmospheric, and tidal perturbations were modeled for a 6U CubeSat with a mass of 11 kg. CAD models for each configuration were developed and served as inputs to map instrument, radiator, and solar panel surfaces used in the view factor calculations. An instrument FOV was created using FreeFlyer modeling objects that feature line-of-sight functions used in scripting an obstruction sub-routine. At each timestep in eclipsed orbit, the function is called to log the time of intersection between the Earth and the instrument FOV object.

The obstruction plots provide two examples of output from the simulation in Figure 23 and Figure 24. The plots are produced from raw simulation data and analyzed to quantify the extent of the obstructions. The plots show the obscurations made by the Earth in the eclipsed region of an ISS orbit throughout the science observation season for the front-facing FOV satellite configuration. As explained previously, the initial orbit RAAN influences the timing of

obstructions. Multiple ISS orbits with varying RAANs were simulated to evaluate the effect on obstruction times.

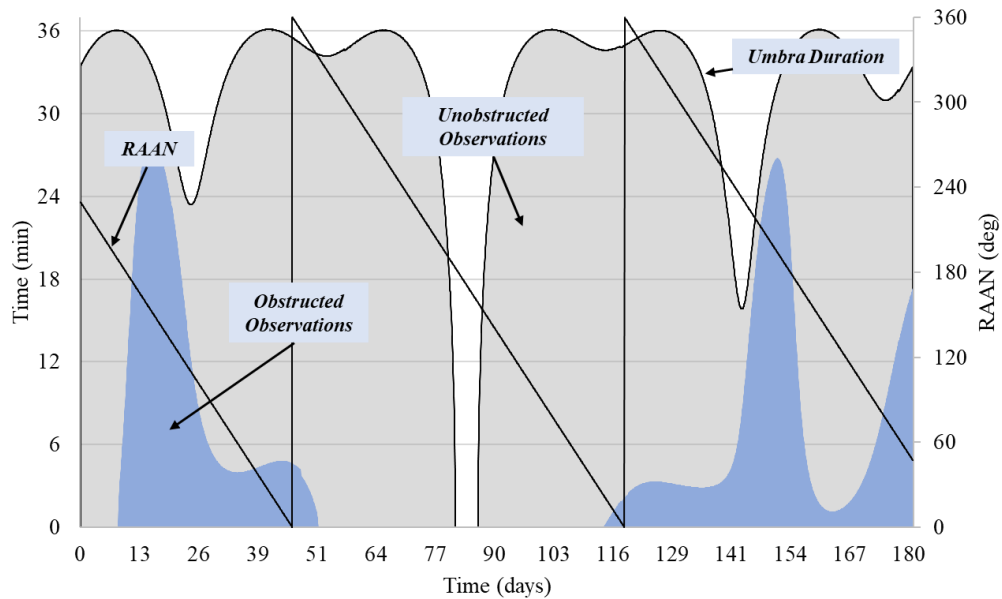


**Figure 23** ISS obstruction profile with initial RAAN of 230 degrees. RAAN has the most significant impact on the timing of the Earth's obstruction of the instrument FOV.

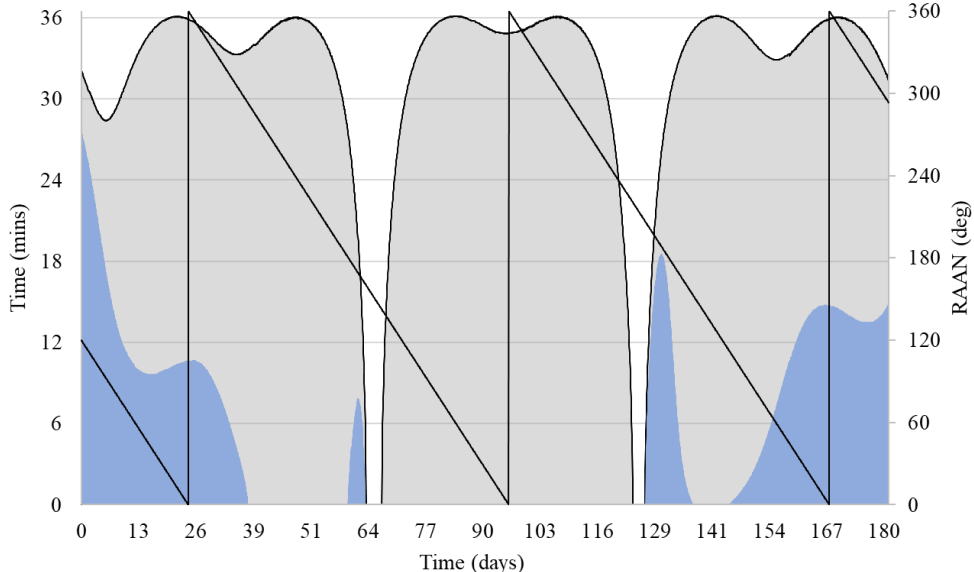


**Figure 24** ISS obstruction profile with Initial RAAN of 120 degrees. Long durations of obstruction occur at the beginning of the science phase in March, preventing imaging opportunities.

The data collected to construct the obstruction profile (shaded in blue) is compiled once per orbit and represents the elapsed time of the obstruction event. The gray shaded area represents the total duration of eclipse compiled per orbit. The difference between the obstruction profile, subtracted from the total eclipse time, is the duration available for unobstructed imaging. This quantity is used to determine if a 15-minute imaging session can be performed on a particular orbit.

In the 230 degree RAAN case (Figure 23), the observation season starts with a clear-sky view without obstructions. In the 120 degree RAAN case, the geometry is not favorable for observations at the start of the science season. These examples demonstrate how obstruction profiles can vary significantly with the initial RAAN. Trials on both the front-facing and side-facing FOV satellite configurations were performed to assess impacts on imaging opportunities. No significant differences in the profiles of obstruction for both configurations were observed.

Figure 25 illustrates the obstruction plots for each satellite configuration simulated over a science season for the ISS orbit case with the initial RAAN at the Vernal Equinox of 45 degrees. The total number of 15-minute imaging opportunities, including imaging in orbits with limited obstructions occurring at the beginning or end of orbit eclipse, was 2,383. Roughly 1,420 of the 2,383 imaging opportunities were in orbits free from any obstruction throughout the eclipse duration. The obstruction profiles evolved similarly for both configurations and were confirmed in additional ISS orbit trials that varied the initial RAAN. Obstructions were simulated from the instrument perspective for instances in March and May and are provided alongside the obstruction plots in Figure 25.

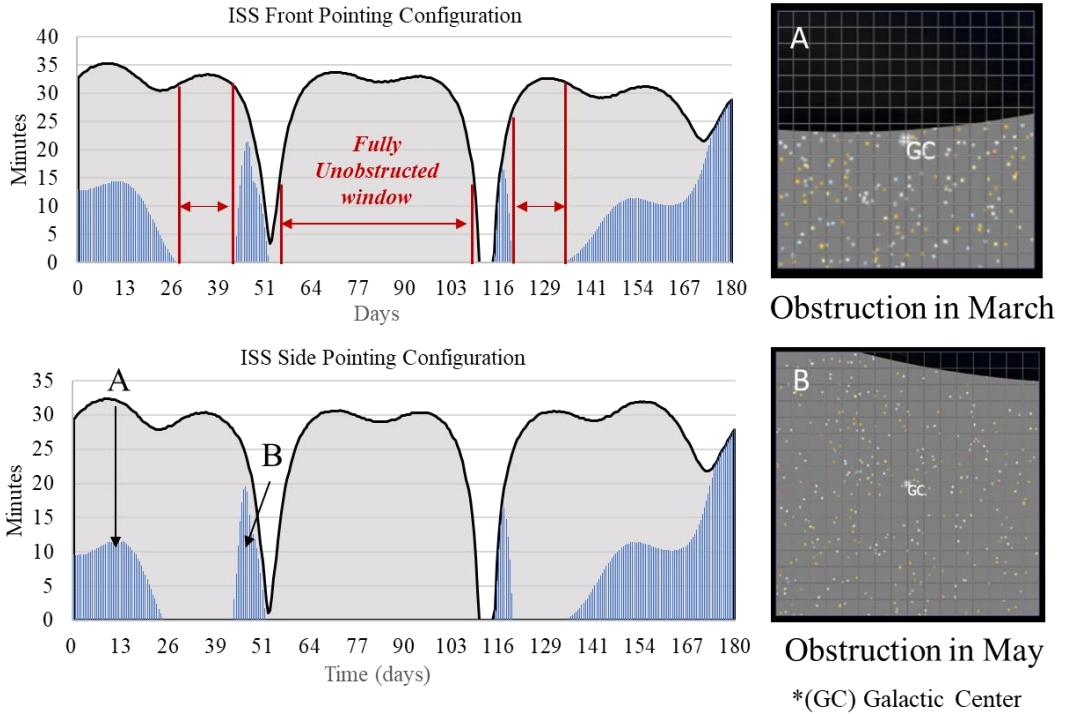


**Figure 25 ISS obstruction profiles with Initial RAAN of 45 degrees. Obstruction profiles of the front and side pointing FOV DarkNESS configurations.**

Obstruction windows that prevented imaging were determined for varying RAAN scenarios for the ISS orbit case. The RAAN directly depends on the time of orbit insertion from the ISS and is not treated as a design variable in this analysis. Table 9 summarizes the number of imaging opportunities and obstruction windows that prevent imaging based on the initial RAAN. Regardless of the initial RAAN, the total fraction of orbits within the science season that are available for imaging is greater than 80 percent, making the ISS orbit a viable option to collect the required 500 images for the mission.

**Table 9 RAAN Variation Impact on ISS Orbit Image Opportunities**

Deployment RAAN	Image Opportunities	No Imaging Opportunities (2023)	Observation Season Imaging Availability
45°	2383	May 6 <sup>th</sup> – 15 <sup>th</sup> July 7 <sup>th</sup> – 15 <sup>th</sup> September 5 <sup>th</sup> - EoM	81.7%
75°	2454	May 12 <sup>th</sup> – 20 <sup>th</sup> July 13 <sup>th</sup> – 21 <sup>st</sup> September 11 <sup>th</sup> - EoM	83.7%
90°	2450	March 21 <sup>st</sup> – 24 <sup>th</sup> May 15 <sup>th</sup> – 23 <sup>rd</sup> July 15 <sup>th</sup> – 24 <sup>th</sup> September 13 <sup>th</sup> - EoM	83.8%
120°	2437	March 21 <sup>st</sup> – 28 <sup>th</sup> May 21 <sup>st</sup> – 28 <sup>th</sup> July 21 <sup>st</sup> – 30 <sup>th</sup>	83.1%
230°	2292	April 1 <sup>st</sup> – 15 <sup>th</sup> June 9 <sup>th</sup> – 16 <sup>th</sup> August 9 <sup>th</sup> – 22 <sup>nd</sup>	82.7%

Obstruction profiles were generated next for SSO orbit cases. A defining feature of this orbit class is the unique coupling of orbital parameters (altitude and inclination) to prevent the orbit geometry from varying with time with respect to the Sun, as illustrated in Figure 26. The coupling altitude and inclination cause the orbit RAAN to recess at a rate equal to Earth's orbital rate about the Sun, resulting in minimal obstruction when applied to the DarkNESS viewing geometry. A specific case of the SSO features a *Local Time of the Ascending Node* (LATN) to impose a local solar time of satellite passage over equatorial latitudes at a designated time. In the case of DarkNESS, a noon LATN was selected for mission analysis. This class of SSO allows the

orbit plane to recess 360 degrees over a year to maintain a favorable geometry for science and other satellite pointing tasks, such as providing uniform solar illumination for power generation.

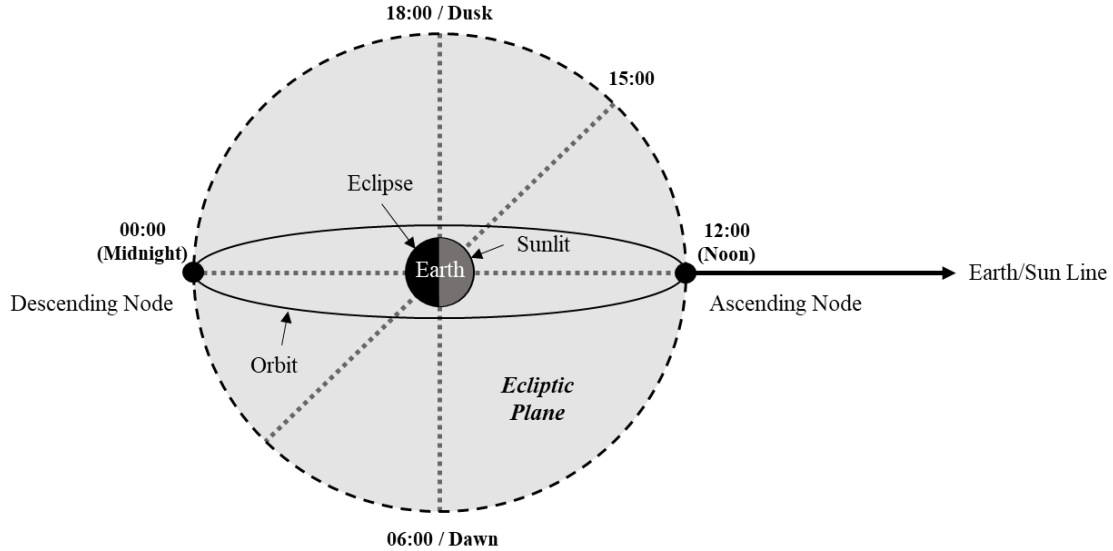


**Figure 26 SSO with an LTAN at Noon.** Sun-synchronous orbits counteract the effect of RAAN regression to preserve the orbit geometry with respect to the Sun.

The SSO obstruction profile was identical for both the front- and side-pointing configurations, as shown in Figure 27. With a RAAN drift rate of 1 degree per day, equal to Earth's rotation rate about the Sun, a consistent orbit geometry minimizes the obstruction of the instrument FOV as the viewing angle remains more favorable throughout the year. A non-favorable satellite viewing angle causes obstructions that occur in March and September in the noon LTAN SSO. Shifting the LTAN can reduce obstruction on one end of the science season (e.g., March) but would consequently increase obstructions on the other (e.g., September). The Noon LTAN SSO offers a balanced orbit option for the DarkNESS mission as the eclipse and sunlit passage times throughout the year are consistent and can simplify the scheduling of satellite tasks. A total of

2,637 image opportunities are provided by the SSO, making it a viable option for the DarkNESS mission.

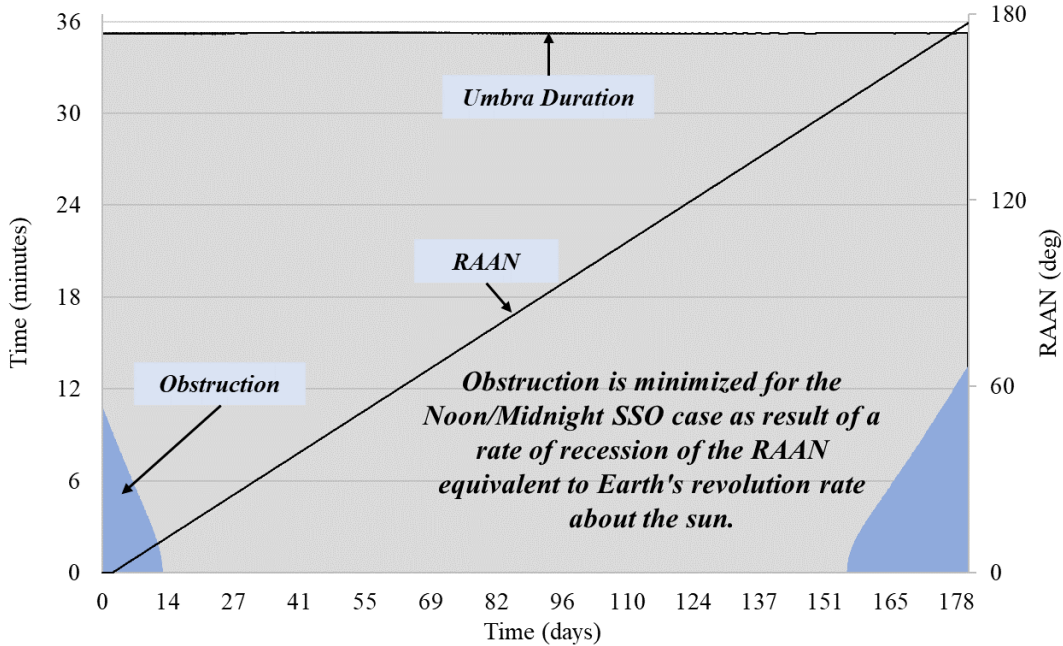


**Figure 27 SSO obstruction profile. Consistent eclipse duration and a long unobstructed imaging window are favorable to the DarkNESS science objective.**

The impacts to imaging opportunities for the ISS and SSO orbit cases are summarized in Table 10. A significant finding is that the obstruction analysis does not favor either FOV configuration and is a function of celestial geometry and orbit viewing angles only.

**Table 9**

**Table 10 Image Opportunities from obstruction Analysis.** Orbit geometry is not a factor in selecting a FOV pointing configuration.

Configuration / Orbit	Image Opportunities
Front-pointing/ISS	>2292
Side-pointing/ISS	>2292
Front-pointing/SSO	2637
Side-pointing/SSO	2637

### **5.3 Earth-Radiator View Factor Analysis**

Orbit analysis is also used to assess radiation exposure on the two DarkNESS satellite configurations. Solar radiation and reflected or emitted radiation from the Earth can induce ambient heating on satellite surfaces that are directly exposed. It is desired to minimize heating on the instrument aperture and the radiator panels to manage the detector operating temperature (170 K). To reduce ambient heating throughout the science season, exposure of the instrument to the sun or the earth must be avoided as much as possible.

Radiator panel performance depends on their geometric orientation on the satellite with respect to the Earth and Sun. In the case of direct solar radiation, exposure to the panels should be avoided entirely. Another challenging design factor is mitigating albedo and Earth's infrared radiation (IR) on the panels. Radiator exposure to the Earth's surface is problematic due to proximity. The exposure of each radiator panel by the earth's surface is dictated by the satellite's attitude, where small changes in viewing angles can significantly alter the portion of the radiator surface in view of the Earth.

View factors are calculated in this analysis from the fraction of surface area that is exposed to the Earth. The exposed surface receives albedo and IR, Illustrated in Figure 28. The Earth-radiator view factor must be minimized and direct exposure to the Sun avoided to reduce this ambient heating. View factor profiles for each configuration were tracked using geometric calculations computed throughout the science season.

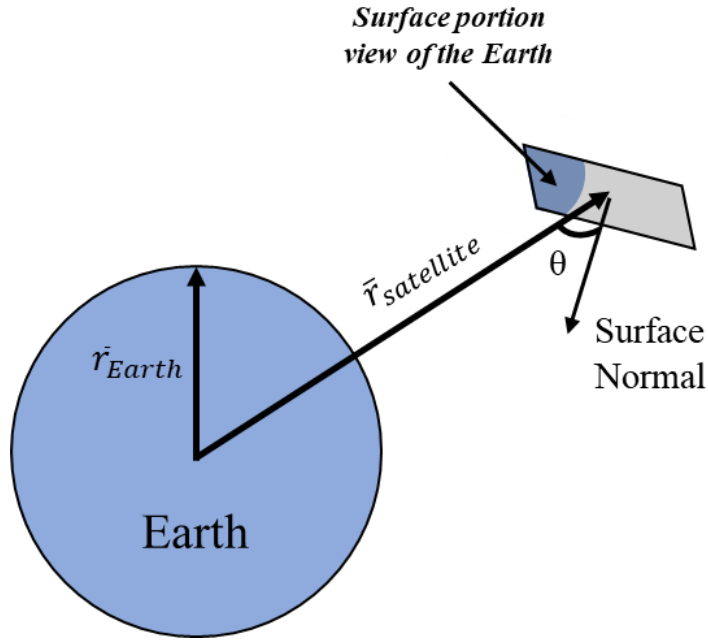


**Figure 28 View Factor.** Geometrical representation of a satellite surface exposure to earth thermal radiation [27][28].

View factor calculations were computed for each satellite surface, defined by a surface normal vector mapped to the DarkNESS configuration CAD model input to FreeFlyer. An example of a view factor measurement is pictured in Figure 29 for the case of the front-pointing configuration in an SSO. The image offers the perspective from the radiator exposed to the Earth while the satellite tracks the sun with the solar panels in a sunlit orbit. The radiator surfaces are denoted Y+ and Y- and correspond to the body frame coordinates defined for DarkNESS. Results for the radiator view factors are plotted over the 180-day science season. As with the obstruction analysis, the same steering algorithm simulates the concept of operations derived pointing scheme.

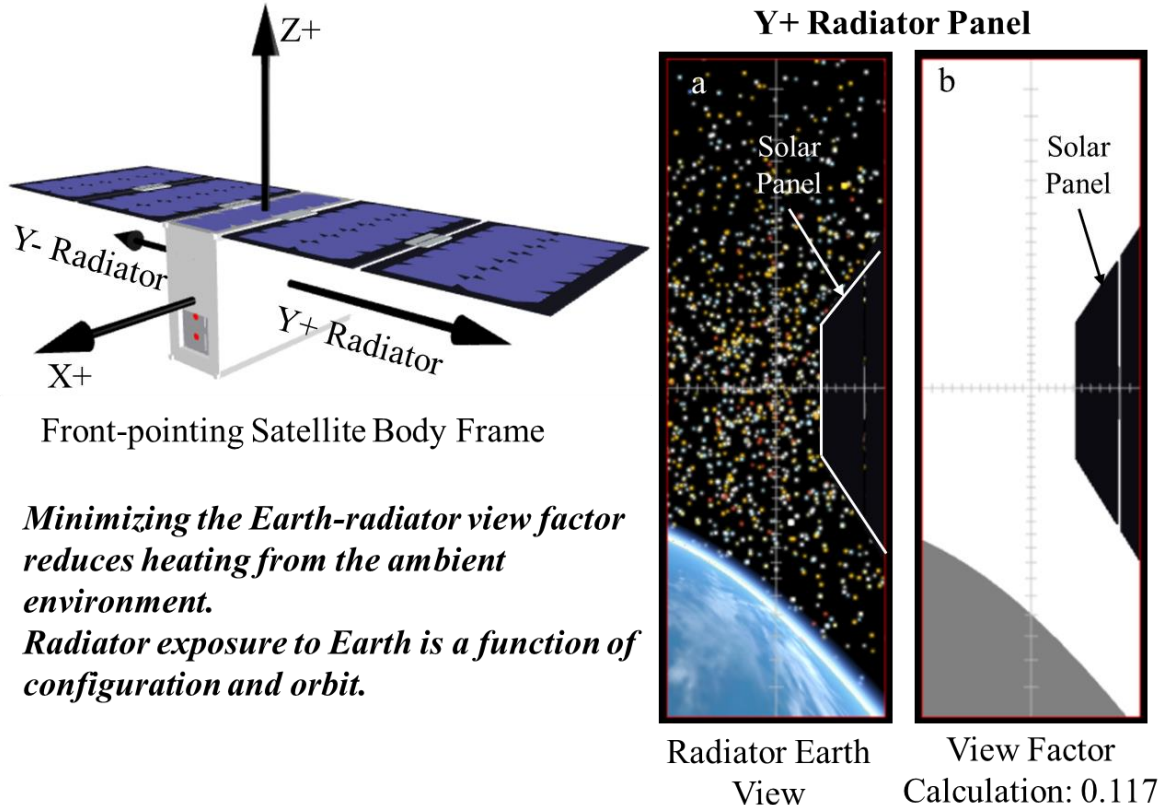


**Figure 29 Earth-radiator view factor. Radiator exposure to Earth for the front-pointing configuration in an SSO in March. (a) Simulated viewpoint from the Y+ radiator panel. (b) The computed view factor, the solar-panel obstruction is computed, but not presented [23].**

Results of the Earth-radiator view factor profiles are shown first for the ISS orbit case in Figure 30. The RAAN regression throughout the science season drives the exposure trends. In both configurations, the radiator surface normal vectors are aligned to the Y+ and Y- body frame axes (as shown in Figure 29), driving a requirement to balance each radiator view factor with the Earth. In the case of the side-pointing configuration, the instrument's alignment to dark space ensures that the Y- radiator has a minimum view factor. However, as interpreted from Figure 30, the Y+ radiator experiences peak view factors exceeding half of the radiator's surface area throughout the science phase, including in mid-June, during the best viewing conditions of the galactic center.

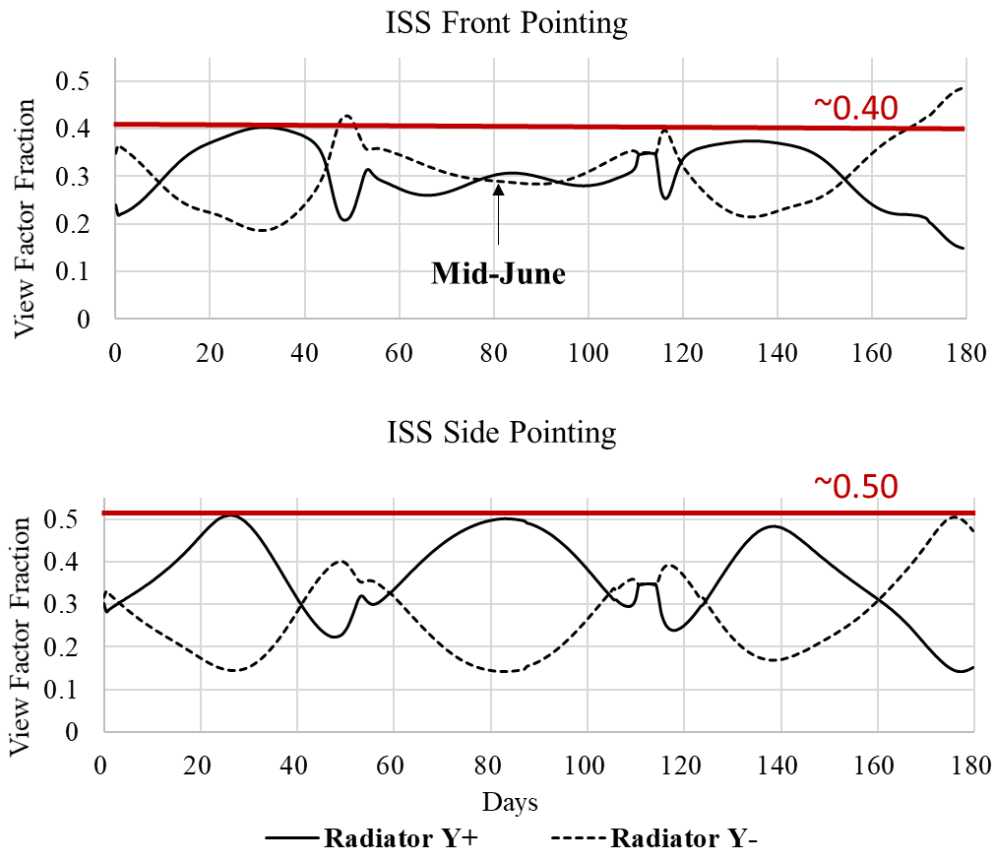


**Figure 30** ISS orbit Earth-radiator view factors profiles. The front-pointing configuration was found to minimize the view factor of the radiator panels.

Figure 31 displays a similar finding for configurations in an SSO. With the RAAN regression rate equal to Earth's orbital rate about the Sun, a smoothed view factor profile is experienced throughout the science season. While the side-pointing configuration can maintain the Y- radiator at a lower and more consistent view factor, the Y+ radiator experiences poor performance throughout the science phase. The front-facing configuration maintains a lower exposure, especially in mid-June, providing more balanced thermal performance throughout the science season.

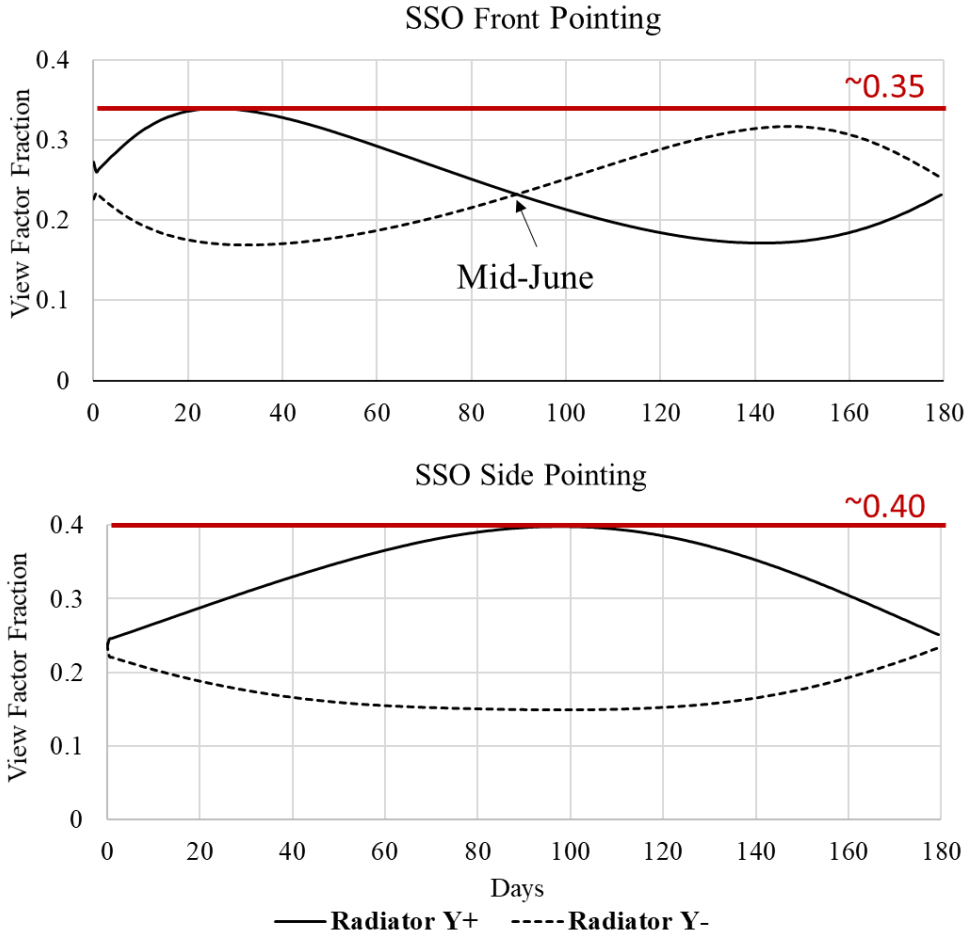


**Figure 31 SSO Earth-radiator view factors profiles. The front pointing configuration was found to minimize the view factor of the radiator panels.**

A summary of findings from the Earth-radiator view factor analysis is provided in Table 11 and lists the peak view factors experienced during the science season. The front-facing configuration was found to out-perform the side-pointing configuration in both the SSO and ISS orbit cases. While satellite configuration resulted in no variation in imaging opportunities, as determined in the obstruction analysis, the front-pointing configuration is better-suited to manage radiator exposure from the space environment. For this reason, the front-pointing configuration was selected for further analysis.

**Table 11 Configuration Performance Summary.** *Radiator view factors favor a front facing FOV satellite configuration.*

Configuration / Orbit	Maximum View Factor
Front-pointing/ISS	~0.40
Side-pointing/ISS	>0.50
Front-pointing/SSO	~0.35
Side-pointing/SSO	~0.40

#### 5.4 Radiator and Aperture Ambient Heating

Thermal analysis is necessary to evaluate the front-pointing configuration's performance in the SSO and ISS orbit environments. It must be shown that this desired configuration can satisfy the thermal requirements defined by the DarkNESS mission, specifically that the instrument focal plane temperature of 170 K can be achieved in either orbit. While an internal radiation model was developed for DarkNESS and included a cryocooler model and internal heat loads, the ambient heating of external surfaces can be evaluated in FreeFlyer and confirms the NX Thermal simulation presented in Chapter 6.

Ambient flux from Earth's albedo and IR can be estimated using view factors and an orbit geometry model. Direct solar radiation from the Sun is also accounted for but doesn't require knowledge of a surface view factor. These three forms of radiative heating are derived from geometry, illustrated in Figure 32, and computed in FreeFlyer by implementing expressions for each radiation source.

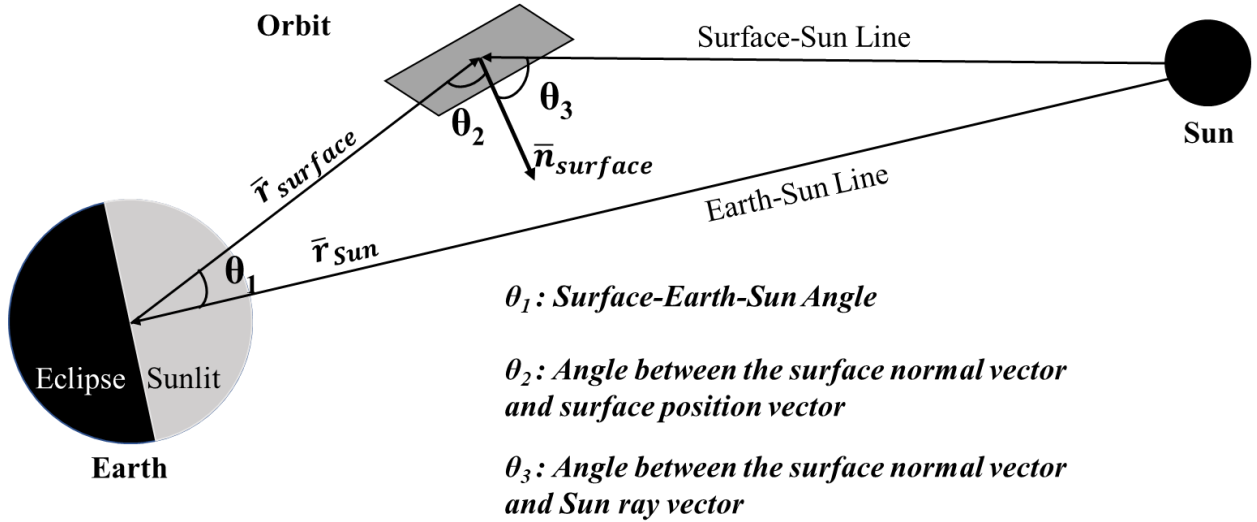


**Figure 32 Radiation Model.** Surface orientation and celestial geometry are used to model direct solar, albedo, and Earth infrared radiation [27].

Heat loads on critical surfaces were modeled by position knowledge obtained in FreeFlyer of the surface with respect to the Earth and Sun. Each surface was oriented by a unit normal vector and mapped to the body frame of DarkNESS, as shown in Figure 33.

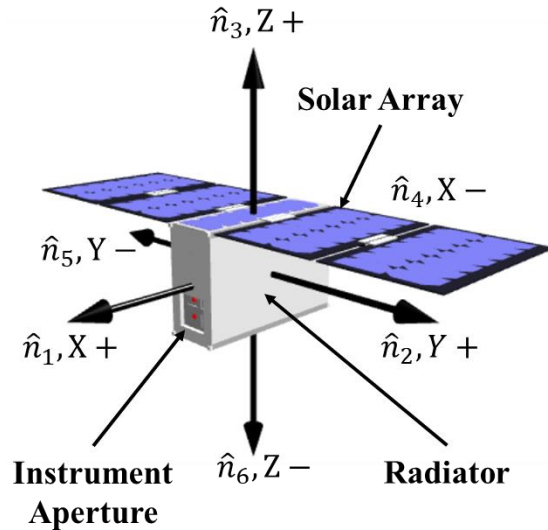


**Figure 33 DarkNESS Surface Normal Vectors and Body Frame.** The coordinate frame is used for thermal view factor analysis.

The heat load induced by direct solar radiation ( $Q_s$ ) is written as Equation 1, where  $G_{sc}$  is the solar constant and represents the direct solar flux at a specified distance from the Sun [27]. This value is calculated based on the satellite position in FreeFlyer. The surface material's solar absorption value ( $\alpha_s$ ) is a model input. For a radiator panel, applying white thermal paint is common to reduce the absorption of ambient radiation and was applied for DarkNESS simulations [38]. From the geometry, the angle between the surface normal vector and Sun position (with respect to the surface center) is found through vector calculus. The cosine of this solar angle models direct solar radiation incidence to the surface. The surface area ( $A_{surface}$ ) is a model input obtained from the DarkNESS CAD configuration.

$$Q_s = \cos(\theta_3) \times G_{sc} \times \alpha_s \times A_{surface} [W] \quad (1)$$

Direct solar radiation is reflected off Earth's atmosphere and surface as albedo radiation. A first-order approximation is written as Equation 2, where knowledge of the Earth-surface view factor ( $f_e$ ) is computed in FreeFlyer [29]. FreeFlyer also provides a function to retrieve the Sun-Earth-Satellite angle ( $\theta_1$ ) used to determine the albedo incidence to the surface. Knowledge of the albedo factor ( $f_a$ ) represents the fraction of direct solar radiation reflected from the atmosphere or surface. Higher-order albedo estimates can be obtained by implementing albedo factor models. An average Earth albedo value of 0.33 was used in this analysis [29][30]. Albedo is not a contributing factor when the satellite is in eclipse.

$$Q_a = f_e \times \cos(\theta_1) \times G_{sc} \times f_a \times \alpha_s \times A_{surface} [W] \quad (2)$$

The surface material's infrared absorption coefficient ( $f_{IR}$ ) is a design variable; an absorption value for white thermal paint was applied to the radiator panels. Earth IR is received throughout the orbit from an emitted flux dependent on the Earth's atmospheric condition and the orbit inclination[27][30]. Earth's average effective blackbody temperature ( $T_e$ ) is 255 K and was used as a first-order approximation in both the SSO and ISS orbit cases [30]. The heat load from Earth IR is also dependent on the Earth-surface view factor shown as Equation 3 [27][30].

$$Q_{IR} = f_e \times \sigma \times T_e^4 \times f_{IR} \times A_{surface} [W] \quad (3)$$

*With Stefan-Boltzmann constant ( $\sigma$ ) in  $\frac{W}{m^2 K^4}$*

The model was used to estimate the total heat load that develops on the radiator and instrument aperture surfaces for the front-pointing configuration. Each surface is computed per simulation time-step and summed as written in Equation 4

$$Q_{surface} = Q_s + Q_a + Q_{IR} [W] \quad (4)$$

Heat loads for the Y+ and Y- radiator panels and the instrument aperture were compiled for the front-pointing configuration in the SSO and ISS orbit environments. Results for the ambient heating of the aperture are provided in Figure 34 and Figure 35. Two complete orbit cycles are shown for March and June for each orbit case through the science season.

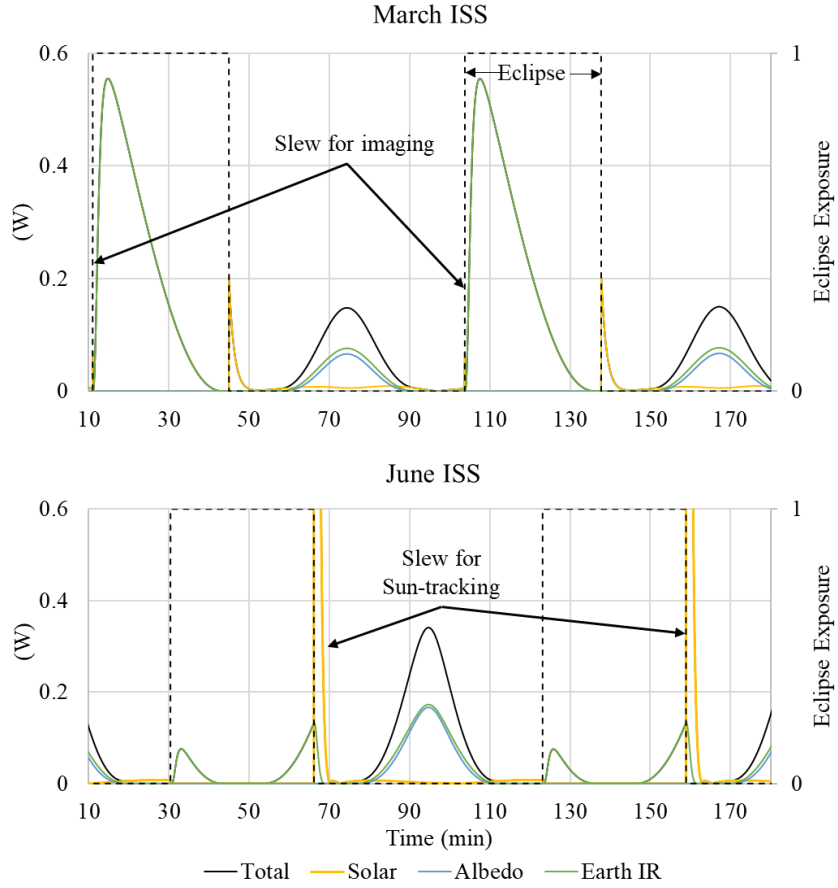


**Figure 34 Ambient Heating of Instrument Aperture in ISS Orbit Environment. The ambient heating of the aperture surface for two orbits in bounding months of March and June.**

Figure 34 displays the two-orbit ambient heating of the aperture face in March and June for the ISS orbit case. Obstruction of the aperture by the Earth in eclipse occurs while DarkNESS attempts to observe the galactic center, resulting in a peak heat load of roughly 0.55 Watts from Earth IR exposure. This heating may be reduced or avoided by scheduling DarkNESS slew maneuvers around the obstruction windows. Any heat load that is induced onto the aperture will negatively impact the instrument focal plane temperature. A peak heat load of 0.15-Watt is seen in the sunlit-orbit driven by the Earth-aperture view factor. Exposure to direct solar radiation is also minimized.

Ambient heating in the SSO case is shown in Figure 35 for the same two-orbit profiles in March and June. Obstruction in March (corresponding to Figure 27) affects the aperture similarly, resulting in a roughly 0.3-Watt load on the aperture surface. The steering algorithm attempts to avoid exposure of the aperture while DarkNESS sun-tracks to generate power in the sunlit part of the orbit. Direct solar radiation on the aperture is avoided, but exposure to albedo and IR generates a 0.4-Watt heat load. Further control schemes to aid in reducing the Earth-aperture view factor can mitigate this exposure and is planned for further study.

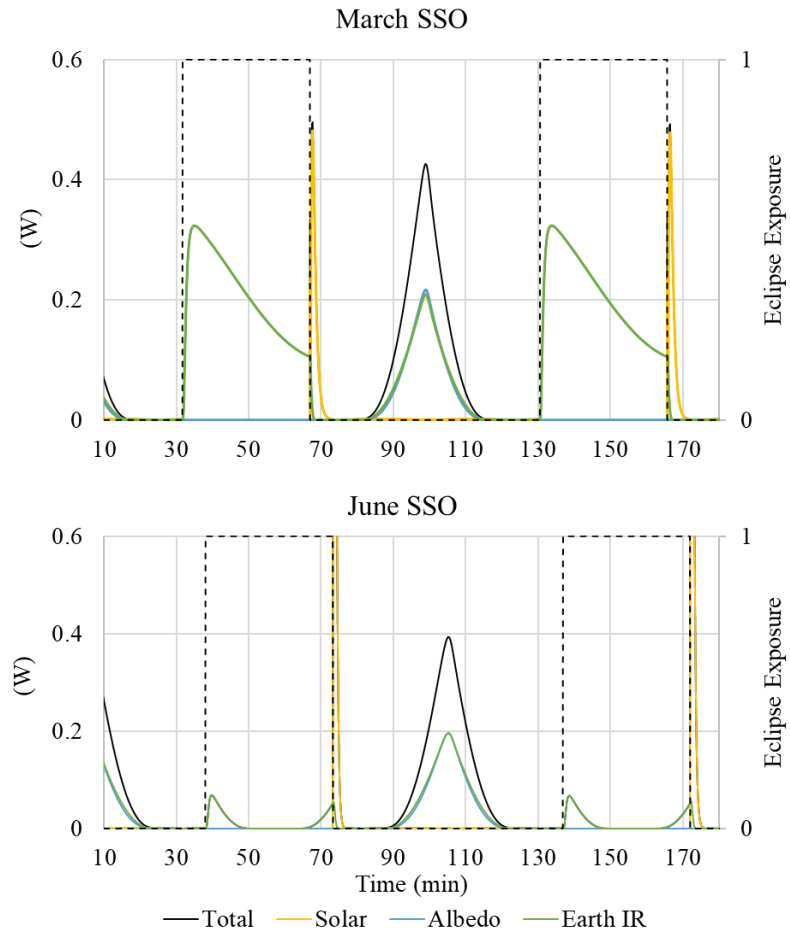


**Figure 35 Ambient Heating the Instrument Aperture in SSO Environment. The ambient heating of the aperture surface for two orbits in bounding months of March and June.**

A summary of the average and peak heat loads for the aperture and radiator surfaces is provided in Table 12. The table also provides the Earth-surface view factors for heat load correlation. Some DarkNESS pointing modes can intermittently induce large heat loads on critical surfaces. Further reducing ambient exposures will involve the implementation of an attitude control scheme that balances the orientation of critical surfaces throughout various DarkNESS tasks (e.g., power generation by sun-tracking and orientation maneuvers scheduled around obstruction events). The trends observed in the analysis serve as an initial set of boundary conditions that will be utilized in the thermal analysis in Chapter 6.

**Table 12 Ambient Heating of Key Surfaces.** *Average and peak values over the science phase are logged for each orbit case.*

Orbit	Surface	Average / Peak View Factor	Average / Peak Heat Load (W)
ISS March	Detector	0.11 / 0.59	0.13 / 0.55
	+Y radiator	0.29 / 0.35	1.18 / 2.5
	-Y radiator	0.28 / 0.58	1.08 / 2.4
ISS June	Detector	0.05 / 0.27	0.15 / 3.26
	+Y radiator	0.28 / 0.43	1.24 / 7.29
	-Y radiator	0.29 / 0.51	1.34 / 8.42
SSO March	Detector	0.10 / 0.340	0.15 / 0.50
	+Y radiator	0.23 / 0.32	0.99 / 9.34
	-Y radiator	0.23 / 0.42	0.98 / 9.23
SSO June	Detector	0.02 / 0.20	0.1 / 3.19
	+Y radiator	0.23 / 0.37	1.02 / 7.17
	-Y radiator	0.24 / 0.81	1.06 / 8.01

## CHAPTER SIX: THERMAL ANALYSIS

### 6.1 Process Overview

The most challenging engineering issue to be solved for DarkNESS is to maintain the temperature of the Fermilab instrument detector at 170 K for the duration of the observation season. The challenge is complicated by orbital geometry, instrument pointing requirements, large cooling power requirements, and limited volume and surface area resources. To address this challenge, a thermal model of the satellite and instrument was constructed to assess the performance constraints that must be satisfied to provide a suitable thermal environment for DarkNESS. The instrument's principal thermal parameters are described in Table 13.

The DarkNESS thermal model approach described in this chapter was initially formulated by a graduate student at the University of Illinois Aerospace Department, Matt Paliwoda. Michelle Zosky, another aerospace engineering graduate student, contributed to the model implementation and performed simulations in Siemen's NX Thermal modeling tool.

**Table 13 Summary of the Constraining Instrument Thermal Parameters**

Performance Requirements	Description	Value
Instrument electrical power input	Payload avionics	10 W
Powered CCDs thermal output	Self-generated heat within the instrument	0.2 W
Electronics operational temperature range	Electronics boards isolated from the detector support structure	-10-40°C
Maximum operational detector temperature	Cryocooled detector required for x-ray observations	170 K $\pm$ 5K (-103°C $\pm$ 5°C)

The thermal model constructed for DarkNESS incorporates an active cryocooler, shown in Figure 36, to chill the instrument CCDs. The cryocooler extracts thermal energy from the CCDs

for transport to external radiators. Passive components such as heat straps and heat pipes then transfer the cryocooler heat load to the radiator panels.

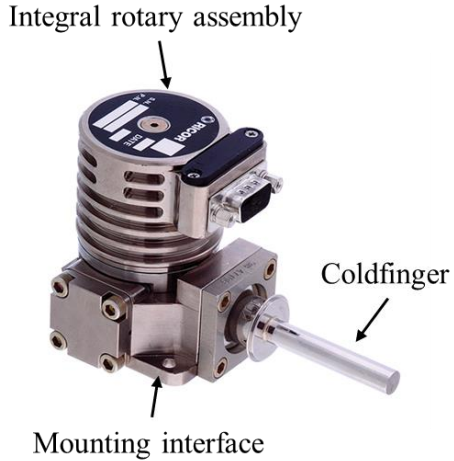


**Figure 36 Ricor K508N Cryocooler considered for the DarkNESS thermal system. The selected cryocooler model is compact and intended for smaller packages systems, including space environment applications [21][31].**

The K508N cryocooler from Ricor was selected for use on DarkNESS for its compactness and greater cooling power rating over other cryocooler candidates. The cryocooler consists of a coldfinger that interfaces to the instrument CCDs through a thermally conductive block. The K508N can provide a coldfinger temperature of 77 K with a maximum cooling power of 550 mW in an ambient environment of 344 K. At the required focal plane temperature of 170 K, a marginal heat load of roughly 1.3 W can be managed in the space environment by the K508N [21].

The K508N requires an average of 9 W of electrical power. The device is operated continuously throughout the science observation period, as the CCD requires a stable operating temperature for imaging over consecutive orbits. A consequence of using a cryocooler for thermal control of the instrument CCDs is the impact on the DarkNESS power budget.

The thermal schematic for DarkNESS illustrates the system's thermal pathways and heat loads, as shown in Figure 37. The thermal characteristics of the satellite's external surfaces (i.e.,

solar panels, radiator panels, instrument aperture) exposed to the ambient environment are estimated in Chapter 5. Direct radiation entering the instrument's beryllium window aperture impacts the instrument CCDs and must be minimized. The satellite receives most ambient radiation on the solar arrays during sun-tracking, with a lower amount impacting the radiator panels.

Much of the heat load on external satellite surfaces are modeled by mechanically interfacing them to the aluminum structural frame. Also interfaced to the satellite frame are internal components representing the internal heat loads coming from satellite subsystem components such as the flight computer and communication radio. While the instrument also mechanically interfaces to the frame, thermal isolation of the CCD assembly from the structure reduces heat transferred conductively from the satellite and instrument electronics.

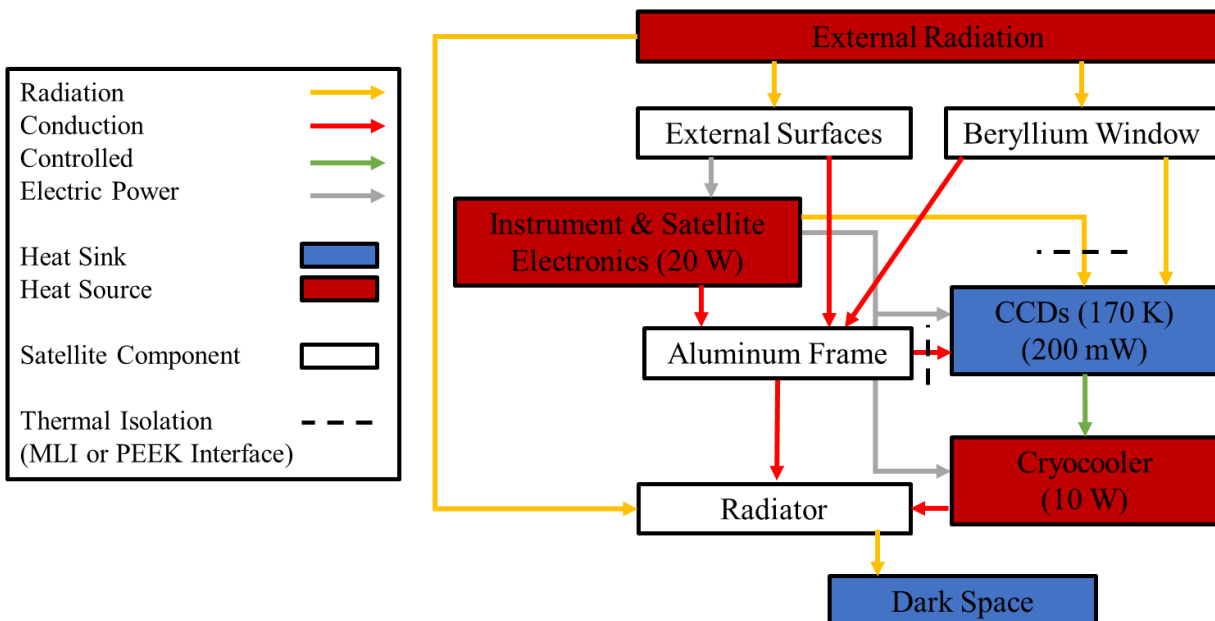


**Figure 37** DarkNESS thermal system architecture. The diagram maps the internal and external loads, thermal pathways, and control devices used in the DarkNESS thermal control system.

External heat loads were modeled using Siemens NX Thermal’s Orbit Heating tool. A CAD model with simplified geometries was built-in Siemens NX and used as the structural input for the thermal simulation, allowing internal heat load objects to be applied to the model. The model was meshed for the finite element analysis to study heat transfer of critical components. Model parameters were selected to model the satellite in an ISS orbit for the beginning of a science observation season in March 2023.

## **6.2 DarkNESS Thermal Model**

The DarkNESS thermal model incorporates the primary structural elements of the satellite in a transient Finite Element Analysis (FEA) to assess the overall performance of the thermal control system. Simulations were performed with simplified geometries to reduce computation times, but enough detail was incorporated into the model to represent necessary thermal and mechanical interfaces accurately. An instrument model, shown in Figure 38, was constructed to provide a high-fidelity representation of the thermal conditions experienced by the instrument detectors.

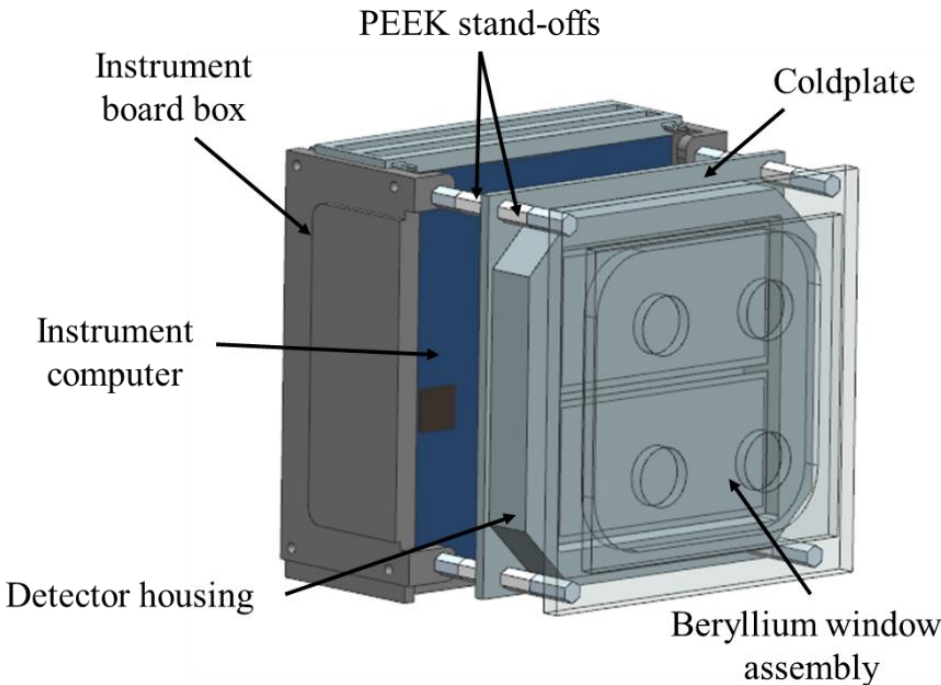


**Figure 38 DarkNESS instrument assembly. Detector focal plane is maintained at 170K.**

The instrument detectors interface to a thin plate (a.k.a., “coldplate”) that serves as a heatsink to transfer the 200 mW heat load produced by the detectors in addition to the incoming ambient heat load from external sources. A beryllium window assembly acts as a filter to reduce lower energy signals from reaching the detectors. The Beryllium window is exposed to the space environment and subject to radiative heating—the coldplate interfaces to a coldfinger extending from the cryocooler. The detector assembly is isolated from the electrical instrument boards by aluminum and Polyether Ether Ketone (PEEK) stand-offs.

The PEEK stand-offs have a low thermal conductivity, isolating the detector assembly from the 10-Watt instrument electrical boards. The electrical boards are enclosed in an aluminum box to transfer heat into the 6U aluminum frame and, ultimately, the external radiator panels. A harness that interfaces power and signal lines from the detectors also serves as a conduit of thermal transfer from the instrument computer.

Though not factored into this analysis, in the final design, Multi-Layer Insulation (MLI) could be used to shield further the detector assembly and the cryocooler coldfinger from internal radiation providing additional margin.

The board box has mechanical and thermal interfaces with the structural frame. Several mounting points and a large surface area contact allow the frame to conduct the 10 W load away from the detector assembly from the instrument boards. The cryocooler is mounted to the structure by a custom aluminum bracket, and a custom copper thermal strap interfaces the cryocooler motor assembly to the radiator panels. Figure 39 shows the instrument integrated into the satellite structure. The internal heat loads of the bus subsystems are marked in red and are concentrated on points of the mechanical interface to the frame. A close-up of the integrated cryocooler and detector assembly used in the thermal simulation is provided in Figure 40.

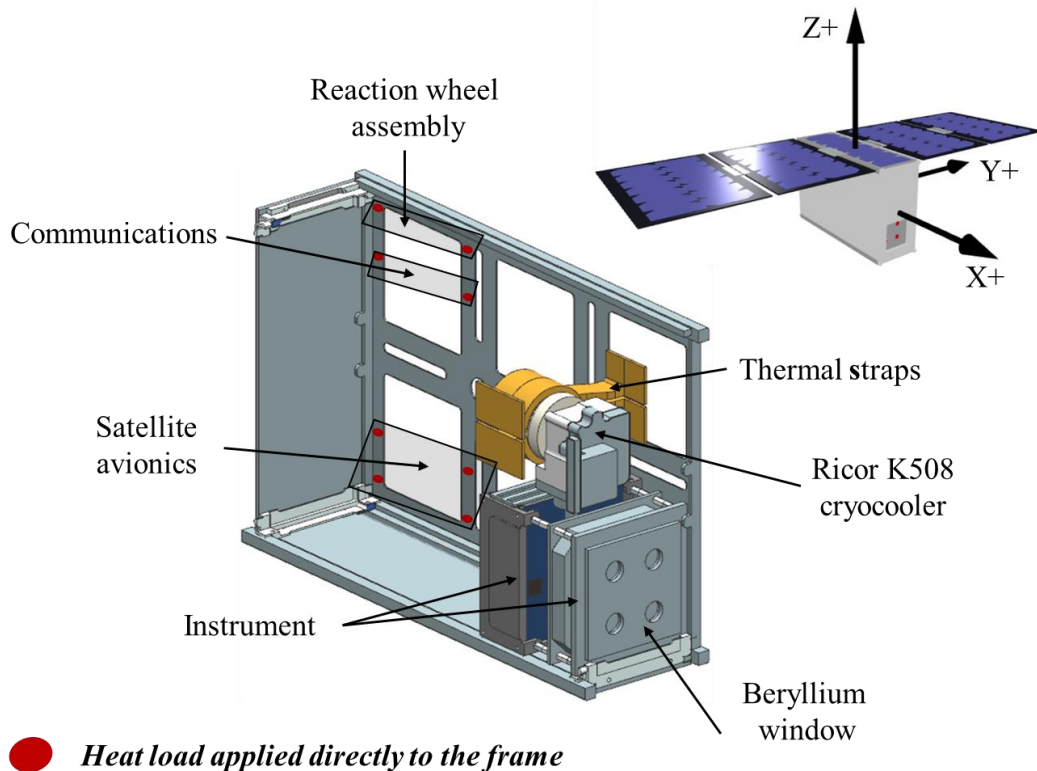


**Figure 39** Instrument and internal satellite subsystem heat loads. The thermal analysis assesses the feasibility of the preliminary system design.

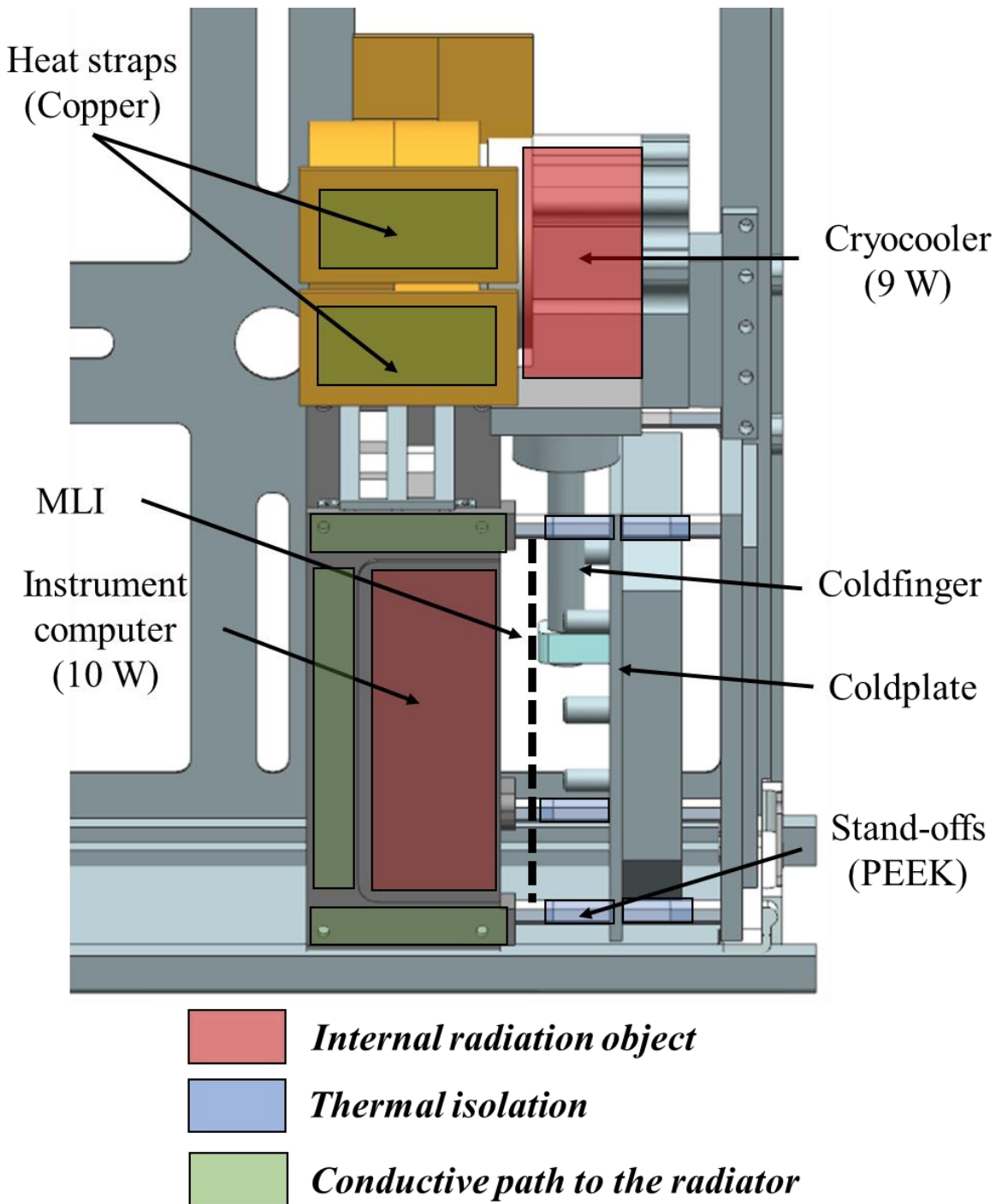


**Figure 40 Thermal model and internal radiation objects used in the thermal simulation. FEA is used to determine if the total heat load develops on the coldplate and detector focal plane. Internal radiation objects are used to simulate heat loads from inside the satellite.**

Internal heat loads were assigned within the thermal model and are listed in Table 14.

Materials were identified for each component, along with the thermal conductivity parameters used as inputs for the model. Total loads are distributed across the structural mounting points.

**Table 14 Internal Heat Loads.**

Internal Heat Loads Applied	Value
Cryocooler cylinder	9W
Payload boards	15W
Avionics boards	4W
Reaction wheels	3W
Communications	1W

Emissivity and absorptivity values, listed in Table 15, were assigned to external surfaces of the satellite and used to calculate ambient heating inputs. The radiator panel, for example, is modeled as a white-painted surface with an emissivity of 0.88 [30].

**Table 15 Structural elements thermal characteristics.** *Emissivity and absorptivity values were obtained for literature and conservatively estimated [27][30].*

External Surface	Emissivity	Absorptivity
Radiator panel	0.88	0.26
Solar array	0.85	0.92
Beryllium window	0.9	0.5
Anodized aluminum	0.84	0.14

An orbital heating simulation in NX Thermal was performed to evaluate the thermal behavior of DarkNESS in LEO. Figure 41 shows the meshed model prepared for the FEA, which was propagated for several orbits. Results for the transient thermal model are analyzed in the following section.

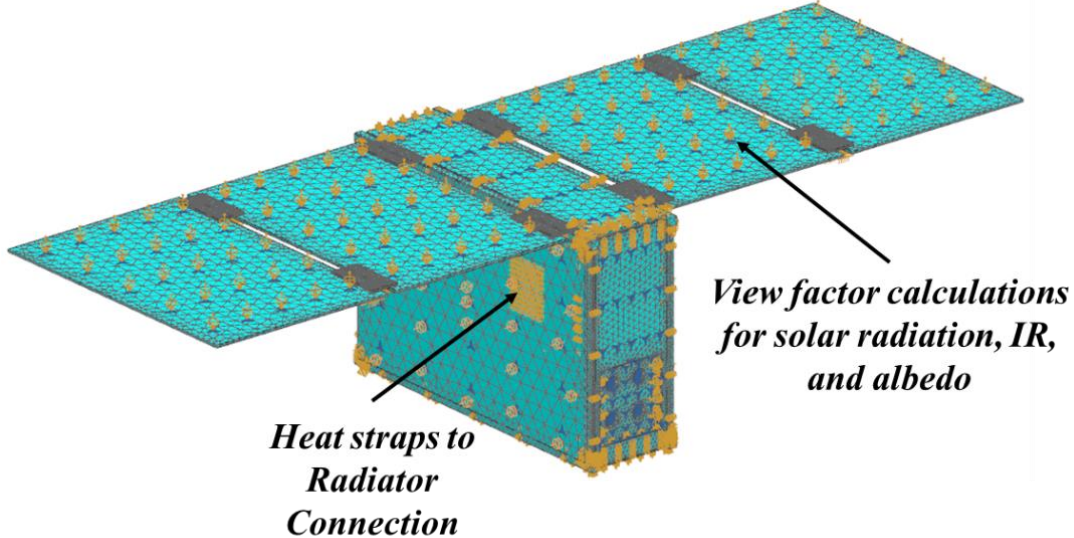
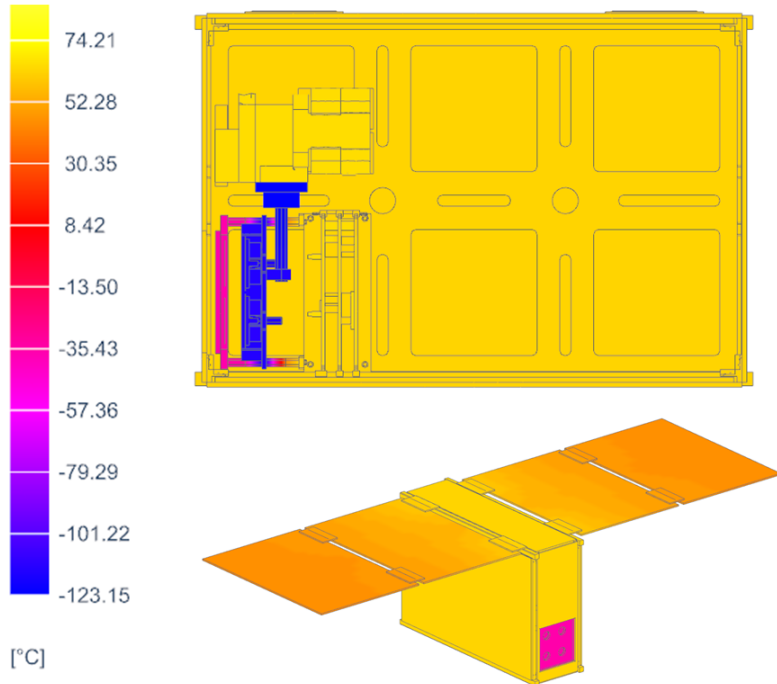


**Figure 41** DarkNESS CAD Model Meshed for Thermal Simulation in NX Thermal. View factors are computed for each mesh element to determine exposure to the orbit environment [32].

### 6.3 Thermal Model Performance Results

Analysis was performed to determine the performance of the thermal control system, as managed by the cryocooler and radiator solution. Satellite thermal states are shown in Figure 42 for the Sun-exposed and eclipsed orbit environments, respectively. The cryocooler maintained the coldplate and detectors' temperatures throughout the orbit period. The 9 W heat load produced by the cryocooler motor assembly is a large contributor to the warm radiator temperature in the eclipsed part of the orbit, resulting in radiator panel temperatures of roughly 50°C. The beryllium window assembly maintains a stable temperature of -32°C for several orbits while exposed to dark space.

*In Eclipse*



*In Sun*

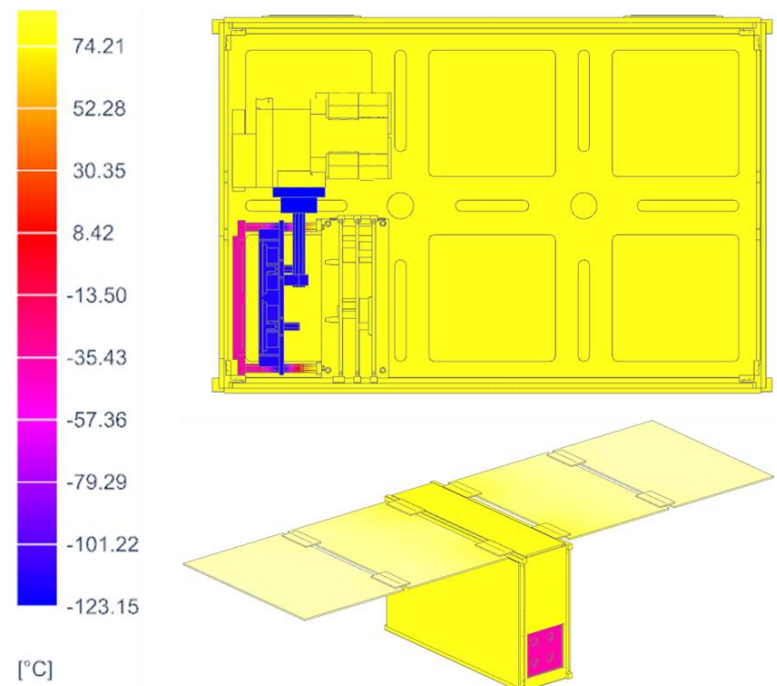


**Figure 42 Eclipsed and Sunlit Thermal Conditions of DarkNESS in LEO Bounded performance results over an orbit period [32].**

The cryocooler maintained the detector assembly within the required temperature range. The PEEK stand-offs reduced the conductive transfer of heat from the warmer instrument electronics, resulting in a gradient of 60°C between the coldplate and instrument electronics box. The cryocooler coldfinger gradient to the coldplate was found to be approximately 2°C. The active use of the cryocooler during ambient sunlit conditions results in a warm radiator temperature approaching 80°C. A cross-section of the instrument is provided in Figure 43 and shows the large gradient across the PEEK stand-offs.

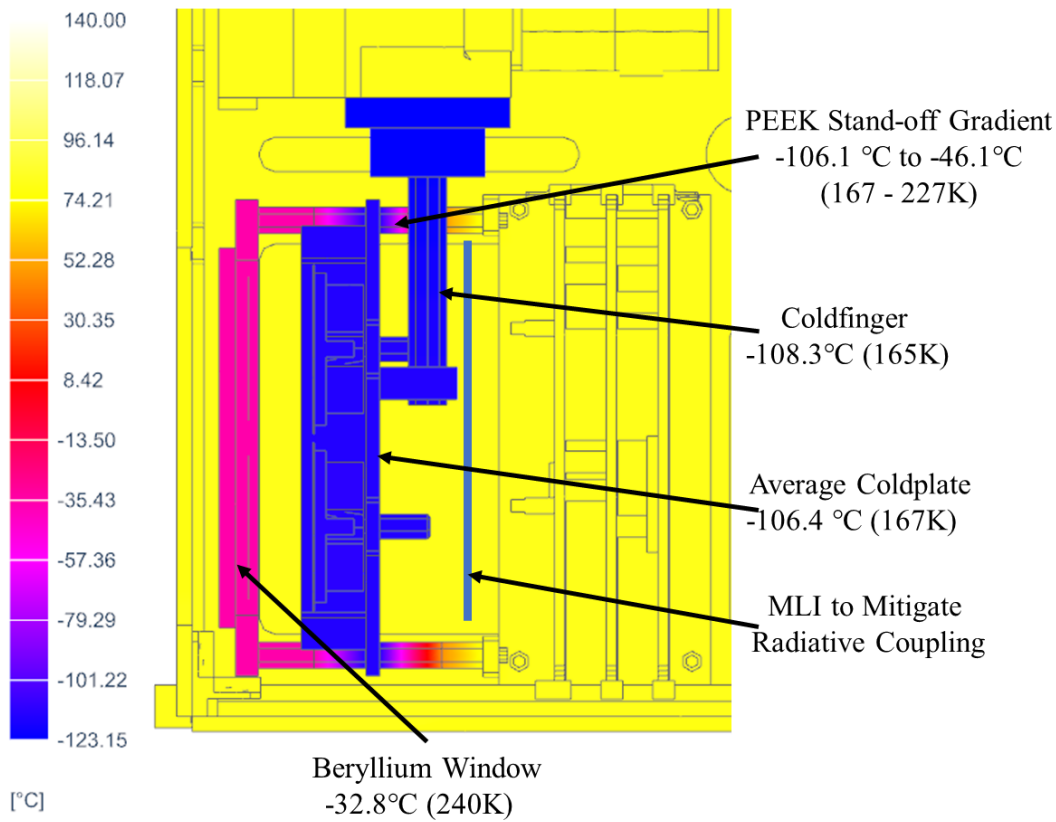
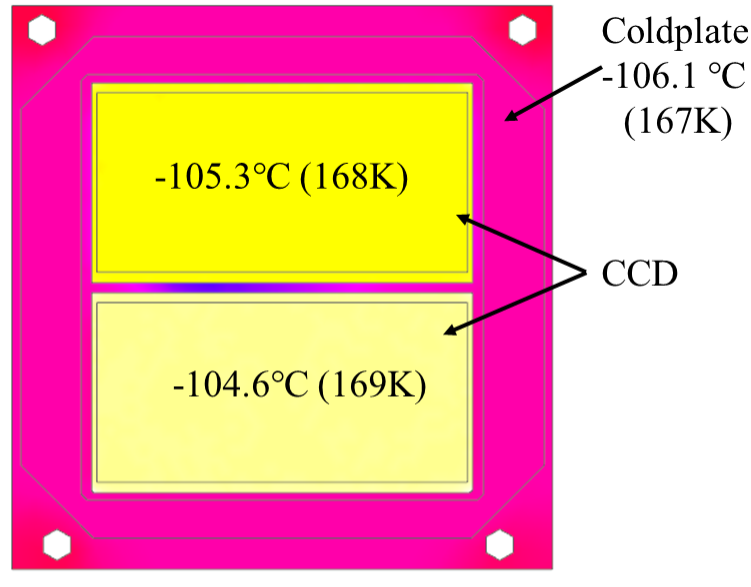


**Figure 43 Cryocooler and detector assembly thermal results. The PEEK stand-offs mitigate heat transfer from the electrical instrument boards, reducing heat load to the coldplate [32].**

An isolated view of the detector is shown in Figure 44 and reveals the thermal gradient across the CCDs and coldplate. Both CCDs are within 5 K of the desired operating temperature. A slight discrepancy between the two CCDs results from the off-centered interface between the coldfinger and the coldplate. The analysis predicts that both CCDs are maintained within the allowed +/- 5-K tolerance. The peak temperatures for critical surfaces during the observation phase are summarized in Table 16.



*CCD temperature requirement of  
170 K  $\pm$  5K is feasible with the  
Ricor K508N cryocooler*

**Figure 44** CCD top-down thermal gradient view. The CCD focal plane temperatures remain in the target requirement [32].

**Table 16 Summary of peak temperatures from key surfaces**

<b>Month</b>	<b>In Sun</b>	<b>In Eclipse</b>
March	Radiator peak: 81.4°C Detector peak: -104.7°C	Radiator peak: 67.8°C Detector peak: -104.7°C
June	Radiator peak: 80.1°C Detector peak: -105.0°C	Radiator peak: 63.8°C Detector peak: -105.1°C
September	Radiator peak: 81.1°C Detector peak: -103.8°C	Radiator peak: 67.1°C Detector peak: -104.4°C

# CHAPTER SEVEN POWER ANALYSIS

## 7.1 Process overview

DarkNESS is a solar-powered satellite. Solar cells arrayed onto panels deployed on the satellite's exterior are illuminated by the Sun. The power produced by the arrays is then stored on board in batteries for use during eclipse periods. This section presents the power subsystem architecture and the analysis supporting the sizing of the subsystem components, as modeled in Figure 45.

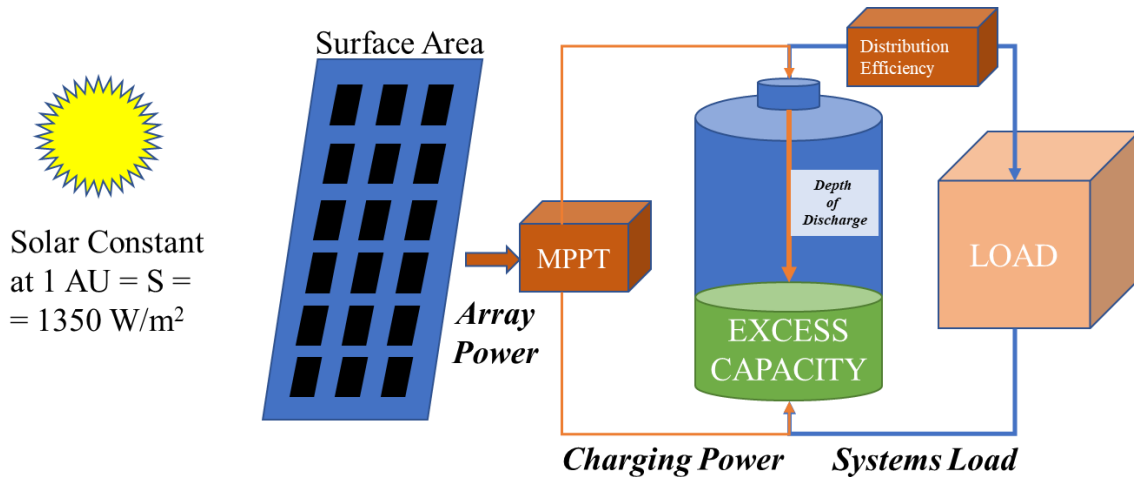


**Figure 45 Power Subsystem Architecture.** The model incorporates solar panels as the generating device to power system loads and charge battery capacity. Maximum Power Point Tracking (MPPT) and power distribution efficiency losses are included in the model.

This analysis determined the number of solar cells required to close the power budget for the DarkNESS mission. The solar array interfaces to an energy storage and distribution system composed of Lithium-ion batteries and an electronics board, together referred to as the Electrical Power System (EPS). Efficiency losses are accounted for in the model and include battery and Maximum Power Point Tracking (MPPT) hardware specifications provided by a component vendor. The analysis incorporated specifications for subsystem components from a commercial

bus provider, NanoAvionics. These components are being considered for application to the DarkNESS mission [33].

## 7.2 Power Subsystem Sizing

A power budget gathers the power requirements for all satellite components, estimates the duty cycle or on-time for each component throughout an orbit, and assigns margins for each component based on the uncertainties in the specifications and duty cycles. The power budget created for DarkNESS is provided in Table 17. A margin of five percent was added to commercially available components with known performance characteristics. For new components that have not yet been built, such as the instrument, 20 percent design margins were applied

The DarkNESS power budget captures the peak electrical power loads which occur during science observations. Averaged for an orbit (i.e., Orbit Average Power), DarkNESS components consume 22.14 W. The instantaneous peak power demand is 68.5 W and occurs during communications sessions with the ground. While this condition persists less than 10 minutes an orbit, the power subsystem must be capable of providing this peak power demand when it occurs.

**Table 17 DarkNESS Power Budget.** Individual component power requirements are summed throughout an orbit; subsystem component power specifications are provided by NanoAvionics [33].

Component	Qnt.	Base Power [W]	Power Margin [%]	Design Power [W]	Duty Cycle [%]	Power Consumption [W]
Flight computer	1	0.330	5.0	0.347	100.0	0.35
Payload controller	1	0.248	5.0	0.260	100.0	0.26
EPS	1	0.150	5.0	0.157	100.0	0.16
Battery heaters	8	2.640	5.0	2.772	10.0	0.28
Magnetorquer set	2	0.799	5.0	0.839	100.0	0.84
Reaction wheels (peak)	1	3.250	5.0	3.413	30.0	1.02
Reaction wheels (nominal)	1	0.425	5.0	0.446	70.0	0.31
Sun sensors	6	0.300	5.0	0.315	100.0	0.32
GPS receiver	1	0.125	5.0	0.131	100.0	0.13
GPS antenna	1	0.066	5.0	0.069	100.0	0.07
IMU	1	1.500	5.0	1.575	100.0	1.58
UHF Rx	1	0.165	5.0	0.173	100.0	0.17
UHF Rx + Tx	1	8.250	5.0	8.663	10.8	0.93
S-band Tx	1	5.000	5.0	5.250	10.8	0.57
S-band Rx	1	0.550	5.0	0.578	100.0	0.58
Cryocooler (steady)	1	8.000	20.0	9.600	100.0	9.6
Payload standby	1	2.000	20.0	2.400	73.1	1.75
Payload imaging	1	10.000	20.0	12.000	16.2	1.94
Payload readout	1	10.000	20.0	12.000	10.8	1.29
					<b>OAP(W)</b>	<b>22.14</b>

A power analysis routine was built using the FreeFlyer astrodynamics software to evaluate solar array and battery capacity sizing for the DarkNESS mission. The power budget serves as an input into FreeFlyer and uses a schedule to determine the power state of each component. An attitude control law was defined to point the solar arrays at the sun when peak power was required. The analysis routine flow is outlined in Figure 46.

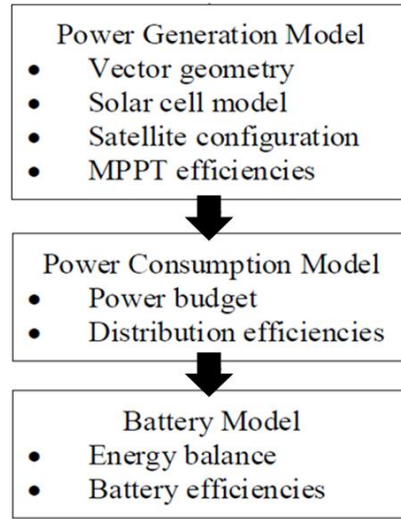


**Figure 46** The power analysis sub-routine flow implemented in FreeFlyer. The model utilizes inputs from the power budget, satellite configuration, and subsystem component models.

Power generation was modeled using knowledge of the sun's position with respect to the satellite. The angle of incidence is required to determine the illumination flux onto the solar cell surface [23]. This geometry is shown in Figure 47.

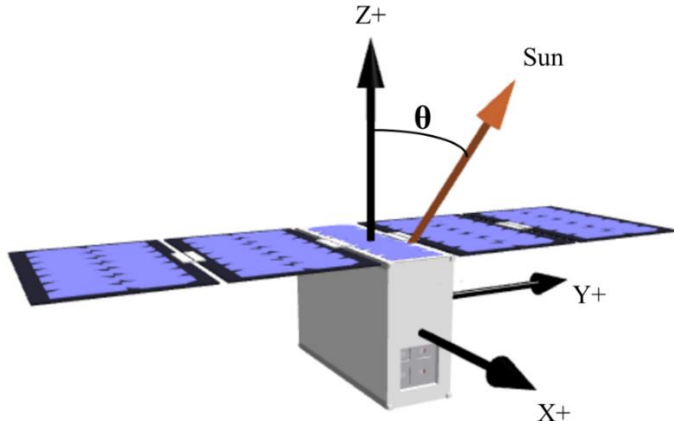


**Figure 47** Angle of incidence used in computing the Sun's intensity onto the solar panel surface. The angle shown is used in the solar panel power generation model [23].

An expression for calculating the power generated by the solar arrays is written in Equation 5 and uses the angle of incidence to determine the intensity of the solar flux ( $G_{SC}$ ) illuminating to solar panel surface [23].

$$P_g = \cos(\theta) \times G_{SC} \times f_{cell} \times A_{cell} \times \left( \frac{R_{Sun}}{\bar{R}_{Sun}} \right) \quad (5)$$

The solar cells used for DarkNESS are commercially available from AZUR SPACE and offer high-efficiency (e.g., 28 percent) in a package sized for CubeSat platforms. An engineering drawing of the cell used for the DarkNESS mission is provided in Figure 48. The effective area of all cells on a panel ( $A_{cell}$ ) is calculated from the individual cell area multiplied by the total number of cells on the array. The solar constant used in this analysis is an average value and depends on several factors. A scaling term is applied to account for the seasonal effect when Earth is either closer or further from the Sun. The day-of Earth-Sun ( $R_{Sun}$ ) distance divided by the average Earth-Sun distance (one astronomical unit in meters) is included in the expression.

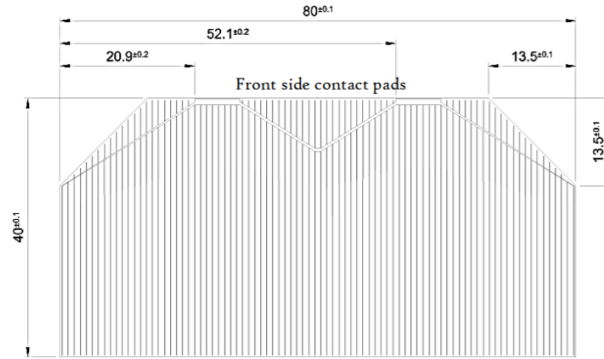


**Figure 48 Engineering drawing of a Solar Cell (TJ Solar Cell 3G30C) from AZUR SPACE used for the DarkNESS mission. Dimensions are in millimeters [34].**

Two available solar panel configurations from NanoAvionics were assessed in FreeFlyer. Options for two (single) deployable panels and two (double) deployable panels were evaluated. Panel parameters and power generation results are shown in Table 18. While the single deployable solar panel configuration satisfied the OAP identified by the power budget, with a healthy margin, the configuration cannot support peak power conditions, providing a peak of only 38.9 W. The

double deployable configuration provided roughly 72 W peak power, meeting the worst-case power demand expected for DarkNESS.

**Table 18 Solar Panel Configuration and Performance.** Available solar panel configurations from NanoAvionics were evaluated in FreeFlyer using AZUR SPACE solar cells. The double deployable solar array was found to meet the peak and OAP required by DarkNESS.

Configuration	Cells	Watts/Cell	Watts Produced	Power/orbit
2 X 1 panel deployed	28 (panel) +5 (body) = 33	1.179*	38.9 W	39 Whr
2 X 2 panels deployed	56 (panel) +5 (body) = 61	1.179*	71.9 W	72 Whr

To completely define the performance of the double deployable solar panel configuration, the solar panels must power the satellite components in the daylight part of the orbit and restore battery capacity consumed in the eclipsed part of the orbit. The energy capacity consumed in the eclipsed part of the orbit was found to be 11.53 Whrs. Approximately an hour is available in daylight to restore the used battery capacity with a charging current of 11.53 W. The breakdown of the elements of the calculation for computing the charging power is provided in Table 19.

**Table 19 Charging Power.** The power generation required by the solar array to restore spent battery capacity from eclipsed orbit

Parameter	Value
OAP in eclipse	22.14 W
Distribution efficiency	96 %
Battery supplied power	23.06 W
Battery capacity spent in eclipse	11.53 Whrs
Charging power in sunlight	11.53 W

The assessment for DarkNESS configured with two double deployable solar panels is presented in Table 20. The previously determined charging power and model system efficiencies are incorporated to determine the overall sizing of the double deployable solar panel configuration. The resulting margin provided by this configuration is 61 percent. This is reasonable for the continued development of DarkNESS; uncertainties in the operation of the cryocooler and instrument design have yet to be resolved.

**Table 20 Solar Array Assessment.** Double deployable arrays satisfy the power budget [33].

Parameter	Definition	Value
OAP Required	Average power required by spacecraft throughout the orbit	22.14 W
Hardware MPPT	The efficiency of the peak power tracker	96.00 %
EPS Output Efficiency	The efficiency of power distribution	96.00 %
Adjusted OAP Required	Adjusted OAP taking efficiencies into account	24.02 W
Power Generation Required	Adjusted OAP Required + Battery Charging Current (11.53W)	40.45 W
Adjusted Power Available	72W X 0.96 X 0.96	66.36 W
Solar Array Margin	Available headroom during sunlight part of the orbit	<b>61 %</b>

The battery capacity required to support operations in eclipse drives the number of battery cells used in the energy storage system for DarkNESS. In addition to capacity from eclipse loads, a Depth of Discharge (DoD) limit requirement is imposed to safeguard the battery cell operating life and maintain adequate voltage output. A DoD of 25 percent was used in this analysis.

The battery cells provided by NanoAvionics have energy capacities of 11.5 Whrs each and are used in pairs [35]. Considering the DoD, a total battery capacity of 46.12 Whrs is required to satisfy DarkNESS requirements. Six cells are needed (rounding up from five) for the battery pack. Two more cells were added to improve capacity to 92 Whrs further to provide additional margin

at this early phase of the program. The cost of adding two cells now is minimal but accommodating them later in the program may not be feasible. The resulting configuration is presented in Table 21. The battery pack provides a nominal output of 7.4 Volts to power DarkNESS subsystems [33][35].

**Table 21 Battery Characteristics and Sizing.** *Sizing of the Battery for DarkNESS based on the required capacity needed to operate in orbit eclipse and depth of discharge limitations to preserve battery life.*

Parameter	Value
Battery energy used in eclipse (OAP*time in eclipse)	11.53 Whrs
Cell capacity	11.50 Whrs
Maximum desired DoD	25 percent
Required battery capacity	46.12 Whrs
Cells needed	5
Cells provided (5 + 39% margin)	8
Actual DoD	13 percent

A summary of the power analysis results is presented in Table 22. A double deployable solar array provides power generation up to 72 W. A total of eight battery cells provides 92 Whrs of energy capacity with adequate margin to maintain flexibility for future instrument and cryocooler design iterations.

**Table 22 Summary of Power Subsystem Sizing for DarkNESS**

Item	Value
2 X 2 panel solar array power generation	72 W
Solar array power margin	61%
Eight battery cells	92 Whrs
Battery DoD	13 %

## CHAPTER EIGHT: DATA AND COMMUNICATIONS

### 8.1 Process Overview

Instrument science data and satellite health and status data are regularly collected by the satellite command and data handling system and stored for downlink to the ground. Satellite telemetry consists of performance information from the flight computer and various subsystems that log the operational state of the satellite. The instrument generates data in two formats. The first data format is a 2.5 KB binned histogram containing condensed information about the raw image produced by the instrument detector during a 15-minute exposure. The binned histogram data is downlinked (on the order of once per orbit) with the satellite telemetry in a package that, with a 25 percent margin, takes up roughly 9.5 KB.

The second data format is the entire raw image produced during a 15-minute detector exposure. The raw image takes up 32 MB and can be requested for downlink by the Fermilab science team based on observations summarized in the associated histogram downlink. Because of the amount of data in the raw image and the limited bandwidth typically available with a CubeSat transmitter, intermittent downlink sessions are required to retrieve the data.

A trade study to size the DarkNESS communication subsystem is presented in this section and enumerates the three possible solutions characterized by available bandwidth. Communication link budgets were derived for UHF, S-band, and X-band communication systems, and the solution options were assessed for the concept of operations compatibility and cost. Options for ground station solutions were also addressed.

Data downlink requirements for the satellite and instrument are provided in Table 23. The satellite telemetry requirement estimated for DarkNESS is roughly 5 KB per orbit and is approximated by estimating the specific data logged for each subsystem.

**Table 23 DarkNESS Data Budget.** *Satellite telemetry and Instrument data drive the communication requirements for DarkNESS.*

Data	Total Bytes per pass
Satellite telemetry	~5 KB
Image histogram	~2.5 KB
Raw image	32 MB
Overhead	25%
Total bytes per pass	~9.5 KB

These data requirements are used to evaluate candidate communication radios to transmit and receive mission data. The link budget presented in this section was produced by Elizabeth Atkinson, a LASSI undergraduate student from the University of Illinois' Electrical and Computer Engineering Department.

## 8.2 DarkNESS Radio Options and Link Budget

Three radio communication downlink systems, Ultra-High Frequency (UHF), S-band, and X-band, were considered in the trade study. Link budgets for each radio band were calculated and are summarized in Table 24.

**Table 24 Communication Systems' Link Budgets.** *Downlink performance summarized for UHF, S-, and X-band solutions [33][37].*

Parameter	UHF	S-band	X-band
Data rate	80 kbps	100 kbps	25 Mbps
Transmit power	1W (30 dBm)	1W (30 dBm)	2 W (33 dBm)
Frequency	401 MHz	2200 to 2290 MHz	8400 MHz
Modulation	GMSK	GMSK	GMSK
Channel	100 kHz	650 kHz	650 kHz
<b>Link margin</b>	<b>4.8 dB</b>	<b>8.4 dB</b>	<b>16.9 dB</b>

The 32 MB raw image downlink is the limiting factor in the analysis. While the 32 MB raw image is not downlinked every orbit, numerous raw images will be downlinked throughout the science observation period, and a timely downlink of the image is desired. A UHF radio from NanoAvionics can downlink 576 KB per ground station pass, with an average pass duration of 500 seconds. As a result, 70 passes are required to complete a single raw image file UHF downlink.

A S-band radio can downlink a raw image every two days (under the condition that up to three adequate ground station passes occur in one 24-hour period). X-band can downlink the raw image in a single pass. The SatLab SRS3 full-duplex S-band transceiver is evaluated for the S-band option in Table 24 and requires lower power and mass than the X-band transmitter. Ultimately, the S-band radio was considered adequate based on the significant cost increase required to incorporate an X-band radio system. Table 25 summarizes the results of the radio system trade study.

**Table 25 Specifications and Costs Summary**

Radio	Total Bytes / Pass	# Of passes to transmit Raw Image	Cost/Unit (Radio Only)
UHF	576 KB/pass	70	~\$8,000
S-band	9 MB/pass	5	~\$12,000 + ground station updates
X-band	6 GB/pass	< 1	~\$40,000 + ground station updates

Communications uplink requirements are considered minimal for DarkNESS. Any one of the three bands considered is sufficient to meet uplink requirements.

### **8.3 Ground Station Options**

Selection of an S-band system for satellite downlink drives ground station requirements.

Options for ground station systems have been reviewed as part of the preliminary design but will require further development in the next phase of the mission development. One option available to the DarkNESS program is the purchase of ground station services from NanoAvionics. NanoAvionics owns and operates ground station facilities domestically and across Europe.

A second option is upgrading the current LASSI UHF ground station at the University of Illinois to support S-band operations. Many commercial ground station kits are available to satisfy this requirement. Third-party ground station services may also be considered in the trade space to determine the most cost-effective solution.

## CHAPTER NINE: CONFIGURATION

### 9.1 Process Overview

This section presents the physical configuration for DarkNESS. The configuration study was performed in Siemens NX CAD software and closely coupled with the thermal and mission analyses presented in Chapters 5 and 6. The CAD model was also used in the thermal and FreeFlyer simulations to establish the required physical constraints. All CAD work shown in this chapter, along with the related CAD models in Chapters 5 and 6, was created by an undergraduate student from the University of Illinois Aerospace Department, Qi Lim. Adam Tlustochowski, another aerospace engineering undergraduate, contributed to the design of the cryocooler mounting bracket.

### 9.2 DarkNESS Mass Budget

The DarkNESS mass budget sums up the mass of all physical components making up the physical satellite. Subsystem components contain margined mass to account for uncertainties in designs that have not matured into finished, measurable products. Many of the subsystem components considered for DarkNESS are available from NanoAvionics. The company provided a complete set of component specifications for DarkNESS [33]. Table 26 provides the detailed list of components and their margined masses identified for the preliminary design of DarkNESS.

**Table 26 DarkNESS Mass Budget.** All DarkNESS components and their respective masses are summed up to provide a preliminary estimate of satellite mass for this design phase.

Component (*estimated)	Subsystem	Vendor	Mass [g]	Qnt	Non-margined Mass [g]	Margin [%]	Total Mass [g]
6U Frame	Structure	NanoAvonics	725.0	1	725	5%	761.3
1x3U bus panel	Structure	NanoAvonics	73.5	2	147	20%	176.4
1x2U bus panel	Structure	NanoAvonics	87.8	1	87.8	20%	105.4
1x2U bus instrument panel	Structure	NanoAvonics	65.7	1	65.7	20%	78.8
2x3U radiator panel	Structure	NanoAvonics	307.6	2	615.2	20%	738.2
Reaction wheel configuration plate	Structure	NanoAvonics	117.0	1	117	5%	122.9
Deployable solar panel	Structure	NanoAvonics	235.0	4	940	20%	1,128.0
Solar cells	Power	AZURSPACE	0.0026	63	0.1638	5%	0.2
EPS	Power	NanoAvonics	190.0	1	190	5%	199.5
Batteries	Power	Panasonic	60.0	8	480	5%	504.0
Flight computer	Avionics	NanoAvonics	102.5	1	102.5	5%	107.6
Payload controller	Avionics	NanoAvonics	110.0	1	110	5%	115.5
Sun sensors	ADCS	GOMspace	0.005	6	0.03	5%	0.0
IMU	ADCS	NanoAvonics	52.0	1	52	5%	54.6
GPS receiver	ADCS	NovAtel	31.0	1	31	5%	32.6
GPS antenna	ADCS	Tallysman	100.0	1	100	5%	105.0
Magnetorquer	ADCS	NanoAvonics	31.0	6	186	5%	195.3
Reaction wheels	ADCS	NanoAvonics	137.0	3	411	5%	431.6
S-band transceiver	RF	SatLab	190.0	1	190	5%	199.5
S-band dual patch antenna	RF	SatLab	49.0	1	49	5%	51.5
UHF radio	RF	NanoAvonics	7.5	1	7.5	5%	7.9

**Table 26 (cont.) DarkNESS Mass Budget**

Component	Subsystem	Vendor	Mass [g]	Qnt	Non-margined Mass [g]	Margin [%]	Total Mass [g]
UHF splitter	RF	NanoAvionics	57.0	1	57	5	59.9
Cabling/harness	Structure	NanoAvonics	517.5	1	517.5	20	621.1
Secondary structural components	Structure	NanoAvonics	1293.9	1	1293.9	20	1,552.6
STLA mainboard	Payload	Fermilab	70.0	1	70	20	84.0
STLA power board	Payload	Fermilab	70.0	1	70	20	84.0
STLA clock board	Payload	Fermilab	70.0	1	70	20	84.0
M3 stainless-steel standoff	Payload	Fermilab	0.006	8	0.048	20	0.1
M3 PEEK standoff	Payload	McMaster-Carr	0.001	8	0.008	20	0.0
Payload avionics box	Payload	UIUC	500	1	500	20	600.0
Detector assembly	Payload	Fermilab	1007.0	1	1007	20	1,208.4
<b>Totals</b>					<b>9692.355</b>		<b>11,134.6</b>

As per the industry standard, a five percent margin was applied to vendor-provided mass specifications. Margins of 20 percent were applied to less mature components such as the instrument hardware and radiator panels, for which detailed design has not yet been completed.

Volume and mass standards have been defined for CubeSats of various form factors (e.g., 3U, 6U, 12U, 16U). Such constraints enable standardized services to integrate CubeSats within deployers carried to orbit by candidate launch vehicles. One such service provider, NanoRacks of Houston, TX, has set an allowable mass of 12,000 g for a 6U CubeSat like DarkNESS [36]. A summary of the mass budget provided in Table 27 shows that DarkNESS falls within this constraint with a total margined mass of 11,134 g.

The budget carries a margin of 865 g or 7.2 percent up to the allowed 12,000 g. The total margined mass (the margins applied to individual components plus the allowed 865 g) was 2,307 g or 19.2 percent of the total allowed mass. This margin is sufficient for the maturation of the design and secondary structure throughout the critical design phase of the DarkNESS mission.

**Table 27: DarkNESS Mass Budget Summary**

Breakdown	Value
Total Margined Mass	11,134.6 g
Allowed Mass	12,000.0 g
Remaining Mass	865.4 g
Remaining Mass %	7.2 %
Mass from Margin	1,442.2 g
Mass from Margin %	14.9 %
Total Mass Margin	2,307.6 g
Total Mass Margin %	19.2 %

### 9.3 DarkNESS Configuration

The instrument form factor and accommodation requirements drive the configuration analysis for the satellite. The instrument is roughly 1U or  $10 \text{ cm}^3$  in volume and has two primary assemblies. The instrument board assembly, responsible for operating the detectors, mechanically interfaces to the 6U bus frame. The board assembly is contained in an aluminum box acting as a thermal sink that conducts heat produced by the instrument boards to the frame and radiator panels. The board box also provides mounting points for the detector assembly, isolated by aluminum and PEEK stand-offs.

The instrument assembly housing the beryllium window and detector packages are fixed only by the stand-offs to the board box to reduce thermal pathways to the detectors. The instrument, shown in Figure 49, is designed by Fermilab and was modified to incorporate the board box for

integration into a 6U CubeSat frame. Space between the two assemblies allows mounting of the cryocooler coldfinger to the underside of the coldplate.

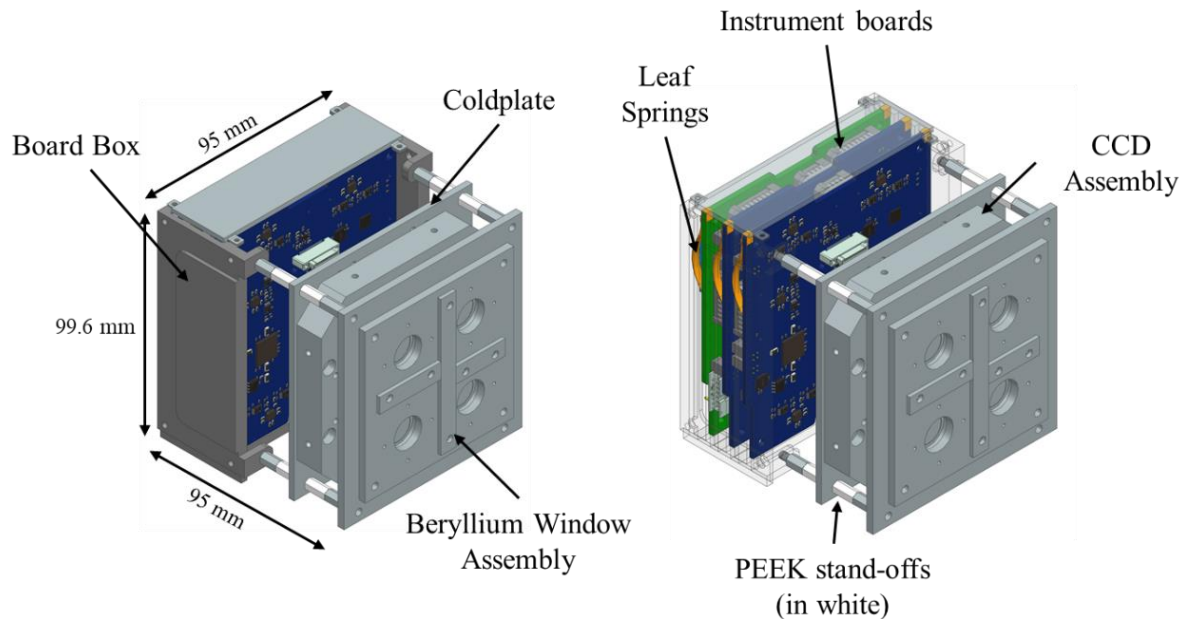


**Figure 49 The DarkNESS Instrument Assembly. The board box provides a rigid base to mount the instrument to the 6U satellite frame.**

The configuration of the selected Ricor cryocooler required its coldfinger to interface at a right angle with the coldplate underlying the detector assembly. As shown in Figure 50, the cryocooler is mounted to the frame by an aluminum bracket. It uses copper heat straps to transfer the heat generated by the cryocooler's motor assembly to the radiator panels. Multi-layer insulation (MLI) is denoted by a dashed line and is used to further isolate the detector assembly from internal radiation produced by the instrument boards and cryocooler.

The instrument and supporting thermal components occupy a 2U portion of the internal satellite volume, with adequate space surrounding the cryocooler to mature the design (e.g., heat strap design, the inclusion of heat pipes). A custom external panel with an instrument aperture cut-out accommodates the instrument FOV and minimizes detector exposure to external radiation.

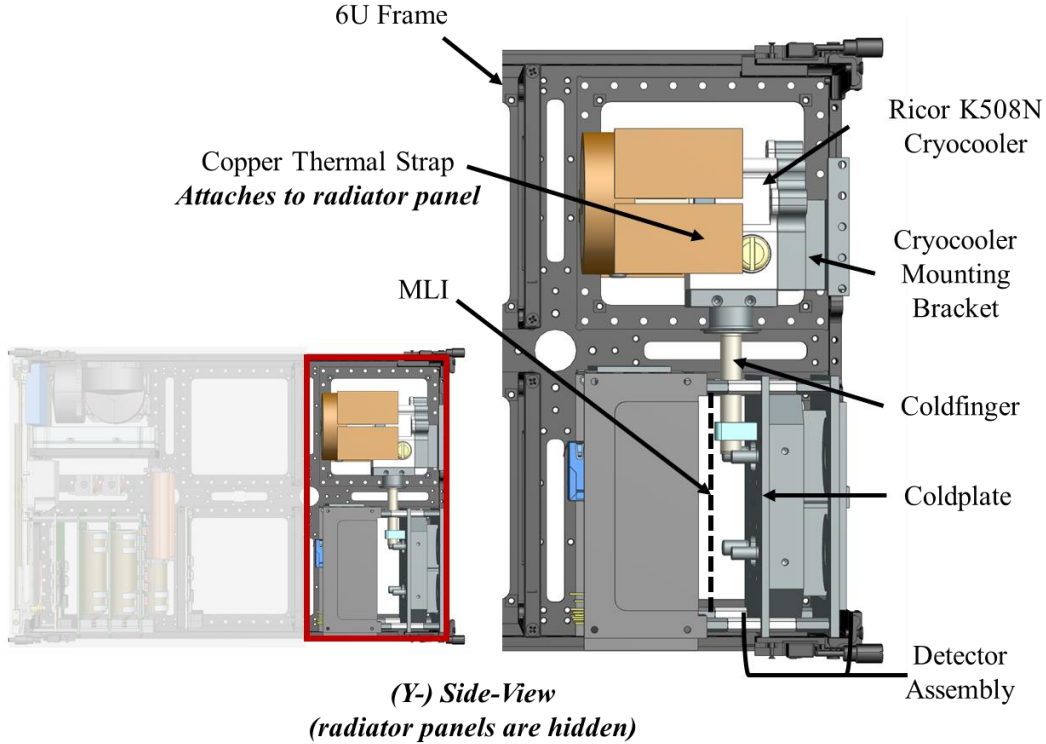


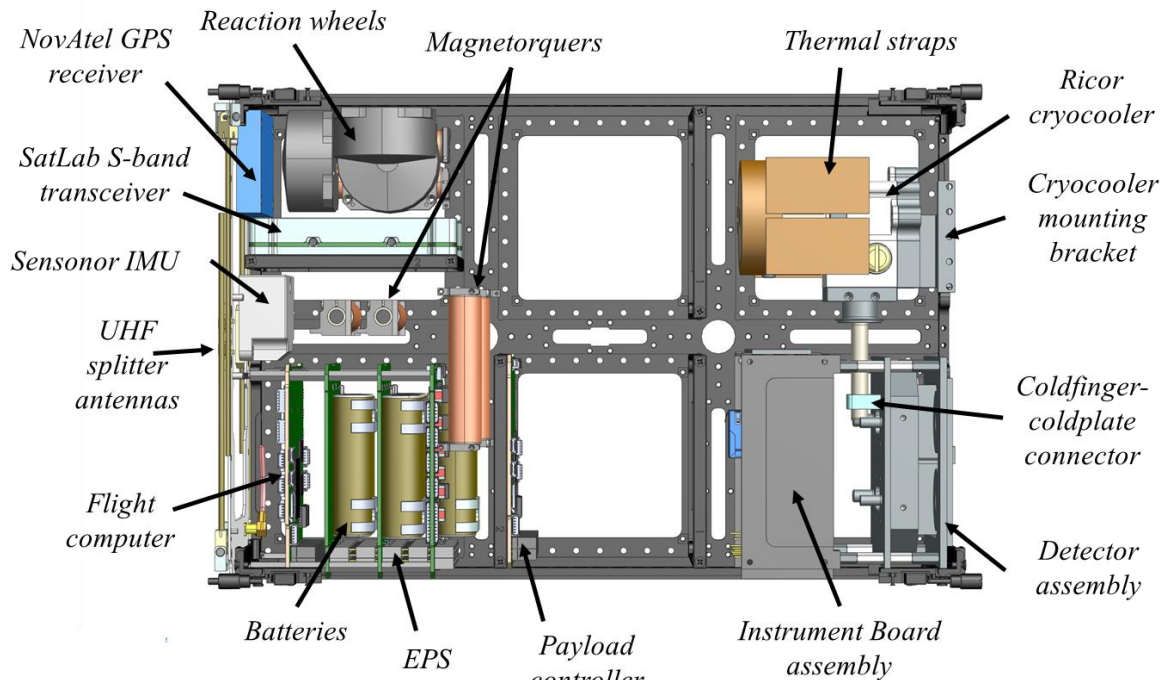
**Figure 50 Instrument integration with the cryocooler model. The active cooling system transfers thermal energy from the detector assembly to the radiator panels [21][32].**

Some components are mounted to the satellite's exterior, such as the S-Band radio antenna and Global Positioning System (GPS) antenna. The S-Band antenna is pointed to a ground station when a communication session occurs. The antenna is located on the (Z-) face of the satellite to allow the detector FOV to remain pointed to deep space (reducing radiation exposure to the instrument). Similarly, the GPS antenna is mounted to the (Z+) satellite face to maintain line-of-sight to the GPS constellation in Middle-Earth Orbit (MEO). In contrast, the radio antenna is pointed towards the Earth's surface.

The location of exterior-mounted components influences the internal configuration as well. The GPS receiver is placed in proximity to the GPS antenna to minimize the length of the radio-frequency cable interfacing it to the antenna. The satellite flight computer is stacked with the EPS and payload control board to reduce electrical connections and mounting points. These three

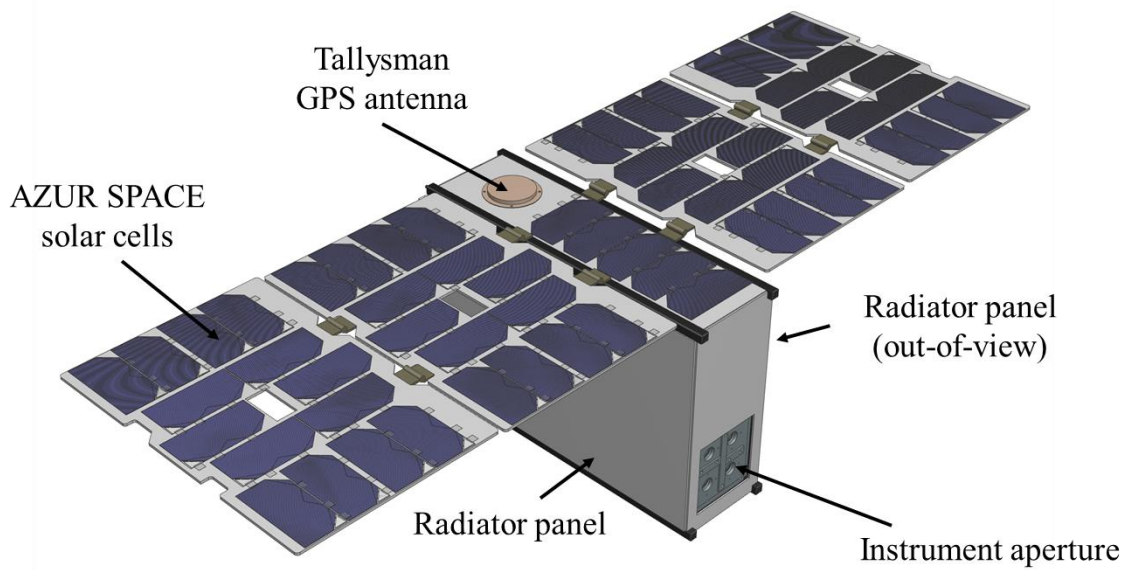
boards are called the “avionics” stack and are situated to reduce the distance to the instrument computer assembly. This allows for a shortened electrical cable run between the avionics stack and the instrument computer.

In the space above the avionics stack, the S-band transceiver is mounted in proximity to its flight computer interface. Reaction wheels are mounted to the frame and provide attitude control for the satellite. Smaller attitude sensors and actuators such as the Inertial Measurement Unit (IMU) and magnetorquers have more placement flexibly. Illustrations of the resulting CAD configuration are provided in Figure 51 and Figure 52. In summary, the configuration of the DarkNESS preliminary design provides for adequate internal volume and mass margins for this phase of the design.



*(Y-) Side-view*

**Figure 51 Interior configuration of DarkNESS Subsystem components. NanoAvionics provide a SatLab S-band transceiver and NovAtel GPS receiver [33][37].**



*NanoAvionics satellite solution for the  
DarkNESS mission*

**Figure 52 Preliminary design for DarkNESS. External satellite configuration satisfies all functional and performance requirements [33][34][40].**

## CHAPTER TEN: CONCLUSION AND ACTION ITEMS

The preliminary design of the DarkNESS satellite mission described by this thesis was presented to the science team at Fermi National Accelerator Laboratory in May 2021, completing the preliminary design review milestone. The review provided a technically sound operational concept and a flow down of verifiable requirements traceable to the mission goals and objectives. The design adopts an acceptable risk level regarding the consistency of technical interfaces with the overall technical maturity. The system design of DarkNESS is well-suited for a 6U CubeSat with subsystem sizing producing adequate technical performance measurement margins.

Integration of a compact cryocooler and the instrument's thermal isolation drove the satellite's internal and external configuration. Mission and thermal analysis revealed that the configuration could support the instrument operating conditions—one challenge facing DarkNESS deals with the large thermal interface between the detector CCDs and the cryocooler. Optimization of the coldplate was identified as a critical driver in the cryocooler's ability to chill the focal plane effectively. Continued work in improving the thermal transport between the CCDs and cryocooler has continued throughout Fall of 2021. The effort will determine the ideal geometry of the coldplate to improve the thermal interface between the cryocooler's coldfinger and the CCD packages.

Steps to include risk mitigation tests to validate the cryocooler and radiator design integration have been initiated with Fermilab. A 6U satellite frame from NanoAvionics and the K508N cryocooler from Ricor has been acquired. These components will be used in a testing campaign to evaluate the thermal performance of the instrument in the thermal vacuum environment. An engineering model will be assembled with radiator and heat straps to acquire data in the laboratory and derive the system identification to characterize the thermal system as

configured on DarkNESS. Laboratory data collected in this manner will aid in verifying the thermal analyses conducted for the program.

Tasks such as evaluating the attitude control performance, verifying mechanical and electrical interfaces between the payload and vendor subsystems, and continued refinements of the cryocooler integration will be completed for the critical design review by Summer 2022. DarkNESS presents a unique opportunity to contribute to the field of astrophysics by providing a low-cost and fast turn-around observatory platform to support a cryogenic X-ray detector. The preliminary design detailed in this thesis is well suited to support Fermilab's science objective in the search for dark matter as a Sterile Neutrino.

## REFERENCES

- [1] Eloise de Castelnau (2018). "Cubesat for Detection of Dark Matter as Sterile Neutrino," Fermilab National Accelerator Laboratory, U.S. Department of Energy Office of Science, The University of Illinois at Chicago.
- [2] Bulbul, Esra, et al. "Detection Of An Unidentified Emission Line In The Stacked X-Ray Spectrum Of Galaxy Clusters." *The Astrophysical Journal*, vol. 789, no. 1, 2014, p. 13., doi:10.1088/0004-637x/789/1/13.
- [3] "Instrument." The Dark Energy Survey, Mar. 2018, [www.darkenergysurvey.org/the-des-project/instrument/](http://www.darkenergysurvey.org/the-des-project/instrument/).
- [4] Dickey, Anna Katherine (2019) "Thermal and Orbital Analysis of DarkNESS CubeSat," ELAIA: Vol. 2, Article 4.
- [5] Dunbar, Brian. "NASA's Great Observatories." NASA, [www.nasa.gov/audience/forstudents/postsecondary/features/F\\_NASA\\_Great\\_Observatories\\_PS.html](http://www.nasa.gov/audience/forstudents/postsecondary/features/F_NASA_Great_Observatories_PS.html).
- [6] Estrada, J., et al. "Focal Plane Detectors for Dark Energy Camera (DECam)." *Ground-Based and Airborne Instrumentation for Astronomy III*, 2010, doi:10.1117/12.857651.
- [7] "Sterile Neutrinos." All Things Neutrino, 2021, [neutrinos.fnal.gov/types/sterile-neutrinos/#moreinfo](http://neutrinos.fnal.gov/types/sterile-neutrinos/#moreinfo).
- [8] X-ray: NASA/CXO/Oxford University/J. Conlon et al. Radio: NRAO/AUI/NSF/Univ. of Montreal/Gendron-Marsolais et al. Optical: NASA/ESA/IoA/A. Fabian et al.; DSS
- [9] Juan Estrada, "Darkness LDRD report Sep 2020", Fermi National Accelerator Laboratory, Report, 2020.
- [10] Rando, N., et al. "Space Science Applications of Cryogenic Detectors." *Nuclear Instruments and Methods in Physics Research Section A: Accelerators, Spectrometers, Detectors and Associated Equipment*, vol. 522, no. 1-2, 2004, pp. 62–68., <https://doi.org/10.1016/j.nima.2004.01.019>.
- [11] NASA, "The Einstein Observatory (HEAO-2)." The High Energy Astrophysics Science Archive Research Center, National Aeronautics and Space Administration Goddard Space Flight Center.
- [12] Christian, D J, et al. "The Einstein Solid State Spectrometer Calibration." The High Energy Astrophysics Science Archive Research Center, National Aeronautics and Space Administration Goddard Space Flight Center.
- [13] "Cryocube-1." NASA, NASA, <https://kscpartnerships.ksc.nasa.gov/Success-Stories/Applied-Technology/CryoCube-1>.
- [14] Putman, Phillip, et al. 2015. "Thermal Management for CryoCube-1," Proceedings of the Small Satellite Conference, Poster Session III, <https://digitalcommons.usu.edu/smallsat/2015/all2015/114/>.

- [15] Wright, Robert, et al. "HYTI: Thermal Hyperspectral Imaging From a Cubesat Platform," 33rd Annual AIAA/USU Conference on Small Satellites, Logan Utah. Digitalcommons, <https://digitalcommons.usu.edu/cgi/viewcontent.cgi?article=4369&context=smallsat>.
- [16] Wright, Robert, et al. "HyTI: Thermal Hyperspectral Imaging from a Cubesat Platform." IGARSS 2019 - 2019 IEEE International Geoscience and Remote Sensing Symposium, 2019, <https://doi.org/10.1109/igarss.2019.8899887>.
- [17] Wright, Robert. "HyTI: High spectral and spatial resolution thermal infrared imaging from a 6U CubeSat" 34 th Annual AIAA/USU Conference on Small Satellites, 2020, Logan, UT.
- [18] Hotbytes.de. "SF070 - AIM-IR." AIM, <https://www.aim-ir.com/en/applications-products/security/cryocoolers/flexure-bearing-coolers/sf070.html>.
- [19] Bruno Mattos, et al.. "The Active CryoCubeSat: System Modeling and Control Design" 35th Annual AIAA/USU Conference on Small Satellites, 2021, Logan, UT.
- [20] Lucas Anderson, et al.. "Active Thermal Architecture: Design and Status" 34th Annual AIAA/USU Conference on Small Satellites, 2020, Logan, UT.
- [21] Integral Rotary Integral Stirling Micro Cooler K508N [Online] November 2021, <http://www.ricor.com/products/integral-rotary/k508n/>
- [22] Krebs, Gunter D. "CryoCube 1 (CC 1)". Gunter's Space Page. Retrieved November 07, 2021, from [https://space.skyrocket.de/doc\\_sdat/cryocube-1.htm](https://space.skyrocket.de/doc_sdat/cryocube-1.htm)
- [23] "FreeFlyer." FreeFlyer Astrodynamics Software, 7.6.0.54542, a.i. Solutions, Inc, <https://ai-solutions.com/freeflyer-astrodynamic-software/>. Accessed 10 Nov. 2021.
- [24] "Galactic Coordinate System." COSMOS - The SAO Encyclopedia of Astronomy, Swinburne University of Technology. Accessed 10 Nov. 2021.
- [25] Cakaj, Shkelzen, et al. "The Apsidal Precession for Low Earth Sun Synchronized Orbits." International Journal of Advanced Computer Science and Applications, vol. 6, no. 9, 2015, <https://doi.org/10.14569/ijacsa.2015.060909>.
- [26] Prussing, John E., and Bruce A. Conway. "Chapter 3: The Orbit in Space." Orbital Mechanics, Oxford University Press, New York, 2013, pp. 46–48.
- [27] VanOutryve, Cassandra Belle, "A thermal analysis and design tool for small spacecraft" (2008). Master's Theses. 3619. <https://doi.org/10.31979/etd.s78d-j9h9>
- [28] Siegel, R., & Howell, J. R. (1996). Thermal radiation heat transfer (2nd ed.). New York: Hemisphere Publishing Co.
- [29] Thornton, Earl A. Thermal Structures for Aerospace Applications. American Institute of Aeronautics and Astronautics, 1996.
- [30] Gilmore, David G., editor. "Thermal Design Analysis." Spacecraft Thermal Control Handbook, 2nd ed., Volume I: Fundamental Technologies, Aerospace Press, El Segundo, CA, 2002.
- [31] Moshe, Barak, et al. "Ricor's K508n Highly Reliable Integral Rotary Cryogenic Cooler." Ricor - Cryogenic & Vacuum Systems.

- [32] “NX Thermal Analysis.” Siemens, Student Version.
- [33] “Nanosatellites and CubeSats.” NanoAvionics, 17 Sept. 2021, <https://nanoavionics.com/>.
- [34] AZUR SPACE Solar Power GmbH, “30% Triple Junction GaAs Solar Cell.” datasheet, 2016.
- [35] “LITHIUM-ION / NNP + HRL TECHNOLOGY.” Panasonic Industrial Devices Sales Europe. [https://www.imrbatteries.com/content/panasonic\\_ncr18650b-2.pdf](https://www.imrbatteries.com/content/panasonic_ncr18650b-2.pdf).
- [36] “NanoRacks DoubleWide Deployer (NRDD) System Interface Definition Document (IDD) 09/20/2017.” Nanoracks.
- [37] SatLab. “SRS-3 Full-Duplex S-Band Transceiver,” CAD, [www.satlab.com/products/srs-3/](http://www.satlab.com/products/srs-3/).
- [38] Eakman, D., et al. “Small Spacecraft Power and Thermal Subsystems.” NASA, Dec. 1994. NASA Contractor Report 19502. McDonnell Douglas Aerospace, Seabrook, Maryland
- [39] IQ wireless GmbH, “IQ SPACECOM S Band Antenna,” datasheet, 2015.
- [40] Tallysman Wireless Inc., “TW2106/TW2108 Embedded Precision GPS L1 Antenna,” datasheet, revision 1.2, 2010.
- [41] Sparke, L. S.; Gallagher, J. S. III (2007). “Galaxies in the Universe: An Introduction”. Cambridge University Press. ISBN 978-0-521-67186-6.
- [42] “Fermilab Fermi National Accelerator Laboratory.” Fermilab, <https://www.fnal.gov/>.